



W. Y. FLOYD LIBRARY  
L. J. JONES SCHOOL  
1900







NPS 68-88-007

# NAVAL POSTGRADUATE SCHOOL

## Monterey, California



# THESIS

557-51

NUMERICAL OCEAN PREDICTION IN THE  
CALIFORNIA COASTAL REGION  
USING A HIGH-RESOLUTION PRIMITIVE  
EQUATION MODEL

by

Clifford D. Johnson

June 1988

Thesis Advisor  
Co-Advisor

Mary L. Batteen  
Robert L. Haney

Approved for public release; distribution is unlimited.

Prepared for:

Chief of Naval Research  
800 N. Quincy St.  
Arlington, VA 22217-5000

T241985

NAVAL POSTGRADUATE SCHOOL  
Monterey, California

Rear Admiral R. C. Austin  
Superintendent

K. T. Marshall  
Acting Provost

This report was prepared in conjunction with research conducted for the Office of Naval Research and funded by the Naval Postgraduate School.

Reproduction of all or part of this report is authorized.

Released by:

EXPENSE

Unclassified

security classification of this page

## REPORT DOCUMENTATION PAGE

1a Report Security Classification <b>Unclassified</b>			1b Restrictive Markings		
2a Security Classification Authority			3 Distribution Availability of Report <b>Approved for public release; distribution is unlimited.</b>		
2b Declassification Downgrading Schedule			5 Monitoring Organization Report Number(s)		
4 Performing Organization Report Number(s) <b>NPS 68-88-007</b>			7a Name of Monitoring Organization <b>Office of Naval Research</b>		
6a Name of Performing Organization <b>Naval Postgraduate School</b>		6b Office Symbol (if applicable) <b>68</b>	7b Address (city, state, and ZIP code) <b>800 N. Quincy St. Arlington, VA 22217</b>		
6c Address (city, state, and ZIP code) <b>Monterey, CA 93943-5000</b>		9 Procurement Instrument Identification Number <b>O&amp;MN, Direct Funding</b>			
6a Name of Funding Sponsoring Organization <b>Naval Postgraduate School</b>		8b Office Symbol (if applicable) <b>68</b>	10 Source of Funding Numbers		
6c Address (city, state, and ZIP code) <b>Monterey, CA 93943-5000</b>		Program Element No	Project No	Task No	Work Unit Accession No
11 Title (include security classification) <b>NUMERICAL OCEAN PREDICTION IN THE CALIFORNIA COASTAL REGION USING A HIGH-RESOLUTION PRIMITIVE EQUATION MODEL</b>					
12 Personal Author(s) <b>Clifford D. Johnson in conjunction with M.L. Batteen and R.L. Haney</b>					
13a Type of Report <b>Master's Thesis</b>		13b Time Covered From To		14 Date of Report (year, month, day) <b>June 1988</b>	
				15 Page Count <b>53</b>	
16 Supplementary Notation <b>The views expressed in this thesis are those of the author and do not reflect the official policy or position of the Department of Defense or the U.S. Government.</b>					
17 Cosati Codes			18 Subject Terms (continue on reverse if necessary and identify by block number)		
Field	Group	Subgroup	PE ocean model, prediction, initialization, Calif coast region		
19 Abstract (continue on reverse if necessary and identify by block number) A high resolution, multi-level, primitive equation (PE) model of the California coastal region is initialized with a temperature field analyzed from real data collected during the OPTOMA11 cruises of June and July, 1984, for the purpose of forecasting the movement of thermal features in the region. The results are compared to the observations and to the forecast experiments of Rienecker <i>et al.</i> (1987), since they initialized their quasi-geostrophic (QG) model with the same OPTOMA11 temperature data. Key prediction features include an anticyclone and cyclone pair, and an offshore 'jet' that was formed between the pair with velocities on the order of 60 cm sec in the upper ocean region (< 225m). The temperature front associated with this 'jet' is traced at the 85m level, in a time series from day 0 to day 14, as is the perturbation pressure field. Translational velocities of this frontal feature are on the order of 5-10 cm sec in a southward direction, which is consistent with those observed. Some quantitative differences between the PE model prediction and the QG model are found. Based on these results, it is feasible that frontal movement in the California coastal region can be forecast by a multi-level, high resolution PE model, given synoptic data for initialization. However, many more studies are needed to understand the dynamics and robustness of the present model predictions.					
20 Distribution Availability of Abstract <input checked="" type="checkbox"/> unclassified unlimited <input type="checkbox"/> same as report <input type="checkbox"/> DTIC users			21 Abstract Security Classification <b>Unclassified</b>		
22a Name of Responsible Individual <b>Mary L. Batteen</b>			22b Telephone (include Area code) <b>(408) 646-3265</b>		22c Office Symbol <b>68Bv</b>

DD FORM 1473,84 MAR

83 APR edition may be used until exhausted  
All other editions are obsolete

security classification of this page

Unclassified

Approved for public release; distribution is unlimited.

Numerical Ocean Prediction in the California Coastal Region  
using a High-Resolution Primitive Equation Model

by

Clifford D. Johnson  
Lieutenant Commander, United States Navy  
B.S., University of Washington, 1977

Submitted in partial fulfillment of the  
requirements for the degree of

MASTER OF SCIENCE IN METEOROLOGY AND OCEANOGRAPHY

from the

NAVAL POSTGRADUATE SCHOOL  
June 1988

---



## ABSTRACT

A high resolution, multi-level, primitive equation (PE) model of the California coastal region is initialized with a temperature field analyzed from real data collected during the OPTOMA11 cruises of June and July, 1984, for the purpose of forecasting the movement of thermal features in the region. The results are compared to the observations and to the forecast experiments of Rienecker *et al.* (1987), since they initialized their quasi-geostrophic (QG) model with the same OPTOMA11 temperature data. Key prediction features include an anticyclone and cyclone pair, and an offshore "jet" that was formed between the pair with velocities on the order of 60 cm/sec in the upper ocean region ( $< 225\text{m}$ ). The temperature front associated with this "jet" is traced at the 85m level, in a time series from day 0 to day 14, as is the perturbation pressure field. Translational velocities of this frontal feature are on the order of 5-10 cm/sec in a southward direction, which is consistent with those observed. Some quantitative differences between the PE model prediction and the QG model are found. Based on these results, it is feasible that frontal movement in the California coastal region can be forecast by a multi-level, high resolution PE model, given synoptic data for initialization. However, many more studies are needed to understand the dynamics and robustness of the present model predictions.

## TABLE OF CONTENTS

I. INTRODUCTION .....	1
A. DESCRIPTION OF THE CALIFORNIA CURRENT SYSTEM (CCS) ...	1
B. HISTORY OF OCEAN PREDICTION IN THE CCS .....	2
C. THESIS OBJECTIVE .....	2
II. THE MODEL .....	4
A. DESCRIPTION .....	4
B. TEMPERATURE DATA AND RESOLUTION .....	5
III. MODEL RESULTS .....	12
A. INITIAL TEMPERATURE, CURRENT AND PRESSURE FIELDS ...	12
B. TIME EVOLUTION OF THE FIELDS .....	16
C. VERIFICATION, COMPARISON WITH QG MODEL .....	18
1. Domain and Initialization .....	18
2. Verification .....	24
3. Discussion and Interpretations .....	26
IV. SUMMARY AND RECOMMENDATIONS .....	30
A. SUMMARY .....	30
B. RECOMMENDATIONS .....	31
APPENDIX A. OPTOMA11 STATIONS, LEG DII, 30 JUNE-10 JULY 1984 ...	33
APPENDIX B. OPEN BOUNDARY CONDITIONS .....	36
A. INTRODUCTION .....	36
B. PROBLEM #1 .....	36
C. PROBLEM #2 .....	38
LIST OF REFERENCES .....	40
INITIAL DISTRIBUTION LIST .....	41

## LIST OF TABLES

Table 1. COMPARISON OF TEMPERATURE (C) .....	7
--	---

## LIST OF FIGURES

Figure 1.	Selected Stations from OPTOMA11, Leg DII, (after Wittmann	3
Figure 2.	Bathymetry of study domain	6
Figure 3.	Model Domain Temperature at 85-Meter Depth	8
Figure 4.	Temperature Profile	10
Figure 5.	Temperature difference between warm anomaly and mean, (Point A)	11
Figure 6.	Input temperature fields at 10, 85, 150 and 225 meters	13
Figure 7.	U,V & P, at 10-meters, Day 0	14
Figure 8.	Sections of Shoreward (U) and Alongshore (V) Velocity, Day 0	15
Figure 9.	85m Temperature front, days 0-14 (two-day intervals, $ci = .5$ C)	17
Figure 10.	85m and 225m P-field evolution days 0, 5, 10 and 14 ( $ci = 2.5$ cm)	19
Figure 11.	Sections of Shoreward (U) and Alongshore (V) Velocity, Day 5	20
Figure 12.	Sections of Shoreward and Alongshore Velocity, Day 14	21
Figure 13.	Model Domains (PE = solid, QG = dashed)	22
Figure 14.	Initial Temperature field and Dynamic Height	23
Figure 15.	Day 6 Verification and Comparison	25
Figure 16.	Day 14 Verification and Comparison	27
Figure 17.	Pressure and Zonal velocities, Day 0, 450m ( $ci = 2.5$ cm, 5cm/sec)	29

## ACKNOWLEDGMENTS

I would like to thank my advisors, Dr. Mary L. Batteen and Dr. Robert L. Haney, for the use of their Primitive Equation model, and for the patience they showed. I would also like to acknowledge Dr. Christopher N. K. Mooers, who allowed me to use the data from OPTOMA11 which made this thesis possible, and Ms. Arlene Bird for her computer help in analyzing the data.





## I. INTRODUCTION

### A. DESCRIPTION OF THE CALIFORNIA CURRENT SYSTEM (CCS)

The California Current is more accurately described as a system because of its broad, filamentous and variable nature. It is essentially the equatorward leg of the North Pacific gyre which is defined by the strong Kuroshio Current on the western boundary, yet the California Current is much less well-defined, as are most true eastern boundary currents. Broad and slow in the mean, its southward trend is often interrupted by offshore "squirts" and meanders which form cold and warm eddies, often in dipole pairs. Chelton (1984) states that the core of the mean California Current is located around 100-200 km offshore in the upper 200 meters, with velocities ranging from 5 to 14 cm/sec depending upon season and location. These velocities are computed geostrophically using 500m as a reference level, i.e., the depth at which the current is assumed to be zero, and using over 30 years of hydrographic survey data from California Cooperative Oceanic Fisheries Investigations (CalCOFI) in the CCS between San Francisco and Point Conception. Velocities up to 40 cm/sec in the equatorward surface current are found further north in the Cape Mendocino region in the summertime, and the current can penetrate as deep as 300-400 meters. The prevailing southward winds force the surface waters offshore due to Ekman drift in the summer season which results in upwelling at places such as Point Sur and Point Arena, bringing up nutrient-rich, colder water from greater depths.

There also has been noted (Hickey, 1979) a poleward undercurrent called the California Undercurrent, with mean velocities of about 5 to 20 cm/sec in summer which lies below and inshore of the southward-flowing California Current. This current can surface during winter months when winds are not controlled by the dominant high pressure of summer over the North Pacific, and it is then known as the Davidson Current.

The CCS is important to the climate of the western coastal states. Although not as well-defined as western boundary currents such as the Gulf Stream, and certainly not as deep, it can bring up nutrients and cold water from the depths during an upwelling event, it can provide "air conditioning" to the beaches from onshore breezes, and it can provide moisture for the surface boundary layer, assisting cloud formation and fog. Fronts associated with temperature, salinity or density gradients form at the boundaries

of the CCS, affecting acoustics performance and the fisheries. The prediction of frontal formation and movement in the California coastal region becomes therefore, an important goal of ocean modelers.

## **B. HISTORY OF OCEAN PREDICTION IN THE CCS**

Most ocean modelers have used seasonal climatology as input data to their models, but the model simulations in these cases cannot be considered ocean predictions. A good example of such a study is that of Ikeda and Emery (1984), who showed that a particular baroclinic jet, typical of that which is observed in the CCS north of Cape Mendocino in the summertime, is baroclinically unstable. Rienecker *et al.*(1987) used observed data to initialize their quasi-geostrophic (QG) ocean model to create a dynamical interpolation and forecast of mesoscale features in the CCS. These initial data were taken from OPTOMA11, the Ocean Prediction Through Observation, Modeling, and Analysis program, which was designed for that very purpose. Six cruises in the same area approximately 180 kilometers offshore from Point Arena were conducted during June and July 1984, each collecting data with XBT drops and CTD casts. Figure 1 depicts the cruise area of one of the legs of OPTOMA11. These cruises were timed to provide synoptic data for initialization and verification of model forecasts. Rienecker *et al.*(1987) were able to make successful dynamic forecasts using a six-level QG model, but the success for some of the time periods required the inclusion of wind stress curl forcing in the model.

## **C. THESIS OBJECTIVE**

With the goal of applying a primitive equation (PE) model to the problem of coastal ocean prediction, I have done essentially the same thing as Rienecker *et al.*(1987), using the data from OPTOMA11 to initialize a PE model of the CCS developed by Haney(1985) and modified by Batteen(1988). From physical considerations and simple scale analysis, it is clear that a multi-level PE model with active thermodynamics has greater potential for coastal ocean predictions than does a QG model, and this is the first thesis to specifically apply such a model to this problem. However, to keep this first study as simple as possible, wind forcing and variable bottom topography are both omitted.

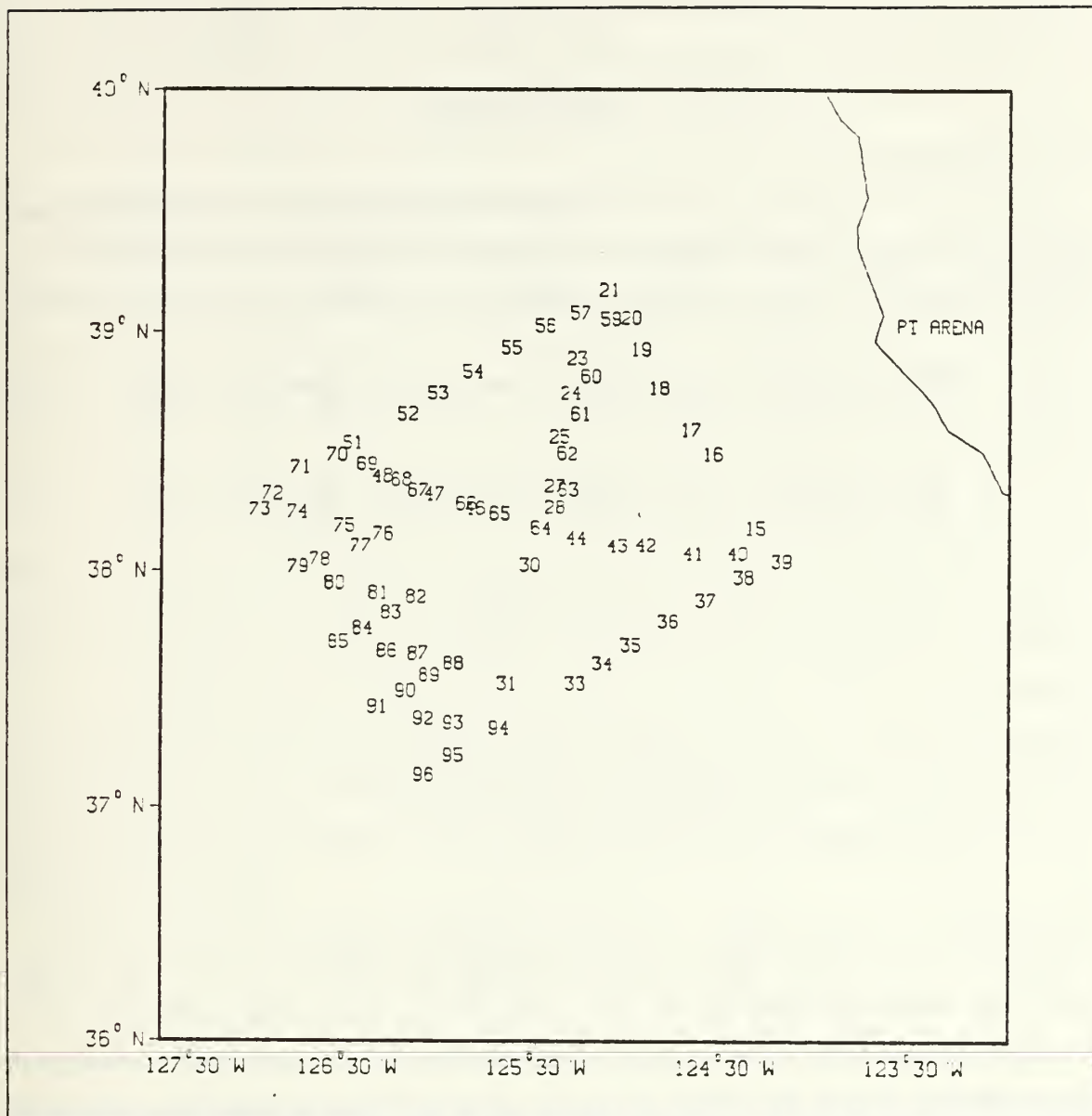


Figure 1. Selected Stations from OPTOMA11, Leg DII, (after Wittmann *et al.*, 1985)

## II. THE MODEL

### A. DESCRIPTION

The numerical model is a ten-level, primitive equation model of a baroclinic ocean on an  $f$ -plane, based on the hydrostatic, Boussinesq, and rigid lid approximations. The governing equations, written in sigma coordinates and standard notation, are as follows:

$$\frac{du}{dt} = \frac{-1}{\rho_0} \frac{\partial p'}{\partial x} + \frac{\sigma}{\rho_0 D} \frac{\partial p'}{\partial \sigma} \frac{\partial D}{\partial x} + f v - A_m \nabla^4 u + \frac{K_m}{D^2} \frac{\partial^2 u}{\partial \sigma^2} + \delta_d(u) \quad [1]$$

$$\frac{dv}{dt} = \frac{-1}{\rho_0} \frac{\partial p'}{\partial y} + \frac{\sigma}{\rho_0 D} \frac{\partial p'}{\partial \sigma} \frac{\partial D}{\partial y} - f u - A_m \nabla^4 v + \frac{K_m}{D^2} \frac{\partial^2 v}{\partial \sigma^2} + \delta_d(v) \quad [2]$$

$$\frac{\partial w}{\partial \sigma} + \frac{\partial u}{\partial x} + \frac{\partial v}{\partial y} = 0 \quad [3]$$

$$p' = D \int_{\sigma}^0 B d\epsilon - \int_{-1}^0 \left( \int_{\sigma}^0 B d\epsilon \right) d\sigma \quad [4]$$

$$B = \alpha g (T - T_0) \quad [5]$$

$$\frac{dT}{dt} = -A_H \nabla^4 T + \frac{K_H}{D^2} \frac{\partial^2 T}{\partial \sigma^2} + \delta_d(T) \quad [6]$$

For the finite differencing, a space-staggered B-scheme patterned after Arakawa and Lamb (1977) is used in the horizontal, and a sigma coordinate system defines the vertical. The boundary conditions at the sea surface consist of no heat flux and no wind stress. At the bottom of the ocean there is also no heat flux, and the stress is computed from the currents in the bottom level assuming a quadratic drag law with an inflow angle of 10 degrees and a drag coefficient of  $1.2 \times 10^{-3}$  (non-dimensional).

The eastern boundary of the model domain represents a straight idealization of the continental shelf of the western United States with a zero-velocity condition imposed, while the northern, southern and western borders are open boundaries which use a modified version of the radiation boundary conditions of Camerlengo and O'Brien (1980). The total depth of the ocean model is a constant (3800m), with the midpoints



of the ten levels located at depths ranging from 10 to 3100m (see Table 1). Figure 2 depicts the actual topography in the model domain, although a flat bottom condition is used in the model. The use of variable topography, and an examination of its effects on coastal ocean predictions, is considered to be a separate study.

## **B. TEMPERATURE DATA AND RESOLUTION**

Development of the temperature input field was done by subjective analysis and interpolation of data from OPTOMA11, Leg DII, which was conducted from 30 June to 10 July, 1984. Seventy-four stations were chosen which were taken between 30 June to 5 July, producing a quasi-synoptic pattern. The data domain (Figure 3) was a rectangle enclosed within latitudes 39.09 and 37.07N and longitudes 124.16 and 127.02W, which covers an area of 31,000 square kilometers, or 203 by 155 km. Final gridpoint resolution in the model was 3.23 km for delta-y and 4.23 km for delta-x, and the data field was framed by borders of 34 km wide on the zonal boundaries and 26 km wide on the meridional boundaries. Final size of the model domain (original data area plus borders) was 271 by 207 km, with the borders being used to blend in the temperature anomalies in various manners which will be discussed later in this section. Each level of the model was represented by 65 by 65 gridpoints. Since observed XBT and CTD data are limited to the upper 450 meters with only a few stations reaching deeper than that (to 735m depth), the bottom four model levels were constructed from the mean and the anomalies at the 450-meter level.

After the observed temperature fields in the area of data, Figure 1, were hand-contoured for the upper six model levels (i.e., those at depths shallower than 450m), a 13 by 13 gridpoint matrix was constructed from each of the resultant contour fields. By using linear interpolation, these matrices were refined to 49 by 49 gridpoint matrices, representing the inside area of Figure 3. The north, south, and western boundaries of the PE forecast model were treated as open boundaries in the manner described by Camerlengo and O'Brien (1980), as stated earlier. To reduce the gradients in the vicinity of these open boundaries (this is not a study of boundary forcing), the temperature anomalies (departure from the average at a given level) were extrapolated from their values at the outer edge of the data region (Figure 3) to one-half that value at the outer margin (model open boundaries).

The eastern boundary of the model was treated differently since it represents a zero-velocity coastal margin. An isothermal condition at each level was desired on this boundary, in order to ensure that the across-shore thermal wind was zero on the coastal

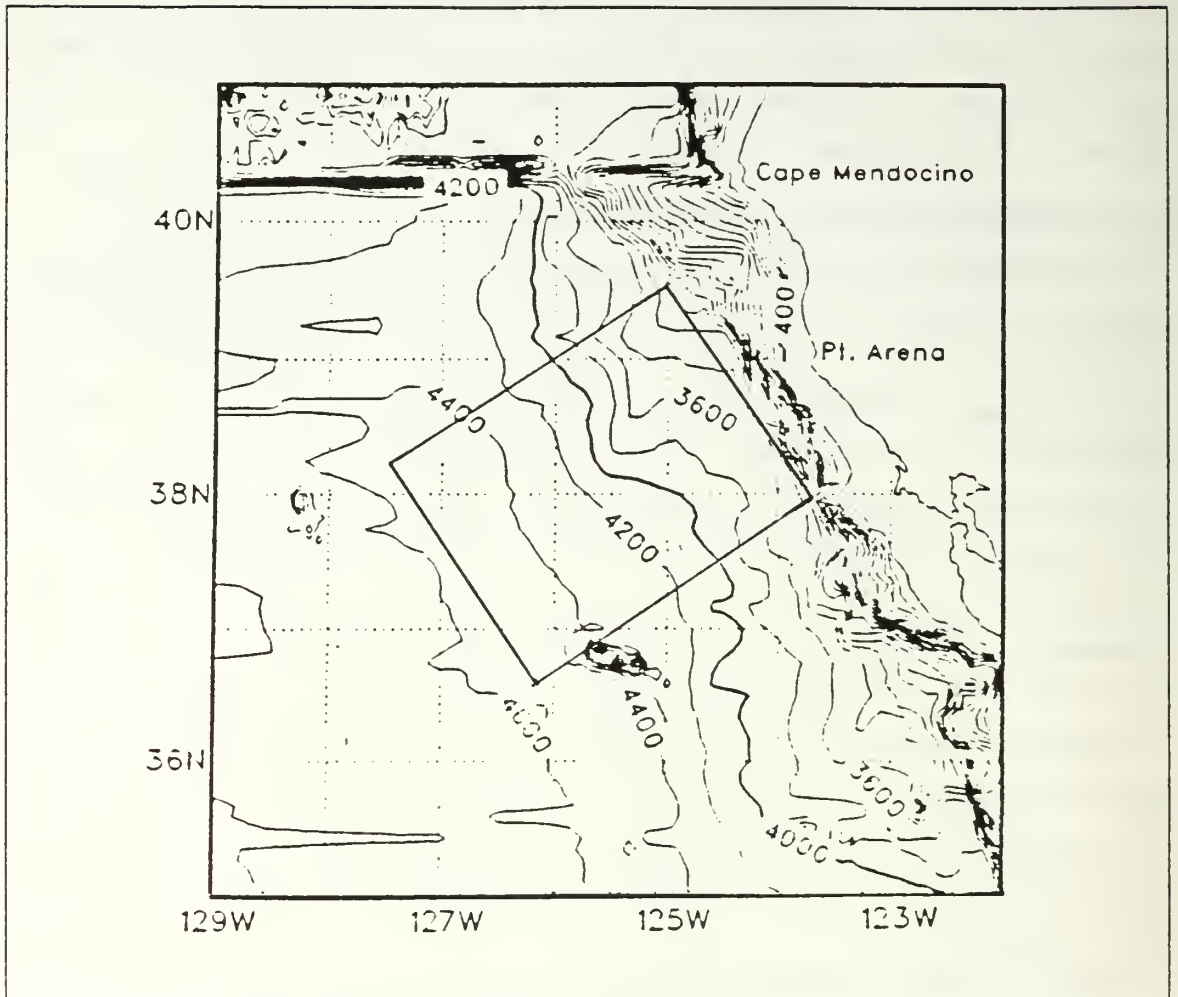


Figure 2. Bathymetry of study domain: (The rectangle represents the PE model domain)

margin. To accomplish this, the alongshore mean of the observed temperatures was calculated at the shoreward edge of the data region (Figure 1) and its across-shore slope was used to extrapolate the mean temperature to the eastern boundary which was located 34km from the edge of the data. The rest of the border was filled in by interpolation between the values at the edge of the data and this extrapolated temperature at the coastal boundary. This procedure was selected from among several possible methods of filling in the data between the coastal boundary and the shoreward edge of the OPTOMA11 observations. The result of applying this analysis procedure at the 85m level is shown in Figure 3. The area of observed data is represented by the inside frame

in this depiction, with the temperature contours superimposed. The contouring outside the framing represents the extrapolation of the data as described above. The main thermal feature at this level is the two-degree temperature gradient in the central-southern portion of the domain, separating the warmer northern portion from the cooler southern portion. This strong thermal gradient is accompanied by a rather intense geostrophic flow, or jet, directed offshore in the center of the domain.

The bottom levels of the model had to be initialized from temperature extrapolations from the deepest model level that contained ample information to make an analysis. The mean temperature of this deepest level, 450 meters, was calculated and extrapolated downward exponentially with a decay scale of 700 meters, to a depth of 3100 meters. The temperature anomaly at this same depth of 450 meters was also extrapolated downward, but using a Gaussian formulation to virtually eliminate any measurable anomaly below 1200 meters. Table 1 displays the calculated temperature means at the various levels and compares these actual values to climatological values that have been used in the absence of real data. Also displayed are the temperatures in the warm eddy

**Table 1. COMPARISON OF TEMPERATURE (C)**

MODEL	DEPTH	MEAN-T	CLIMAT-T	EDDY-T
LEVEL	(meters)	of DOMAIN	(Seasonal)	POINT A
one	10	13.61	14.71	14.45
two	40	12.91	13.89	14.24
three	85	11.24	12.76	12.41
four	150	9.14	11.31	9.85
five	225	7.93	9.88	8.66
six	450	5.78	6.78	6.67
seven	735	4.51	4.54	5.27
eight	1200	3.29	2.90	3.58
nine	1925	2.46	2.18	2.47
ten	3100	2.09	2.01	2.09

noted at point A on Figure 3. The climatological temperatures were used in a modeling study by Batteen (1988), and show a profile decreasing from 15 degrees at the surface to 2 degrees at 4500 meters in an exponential fashion, with no anomaly at all. The actual

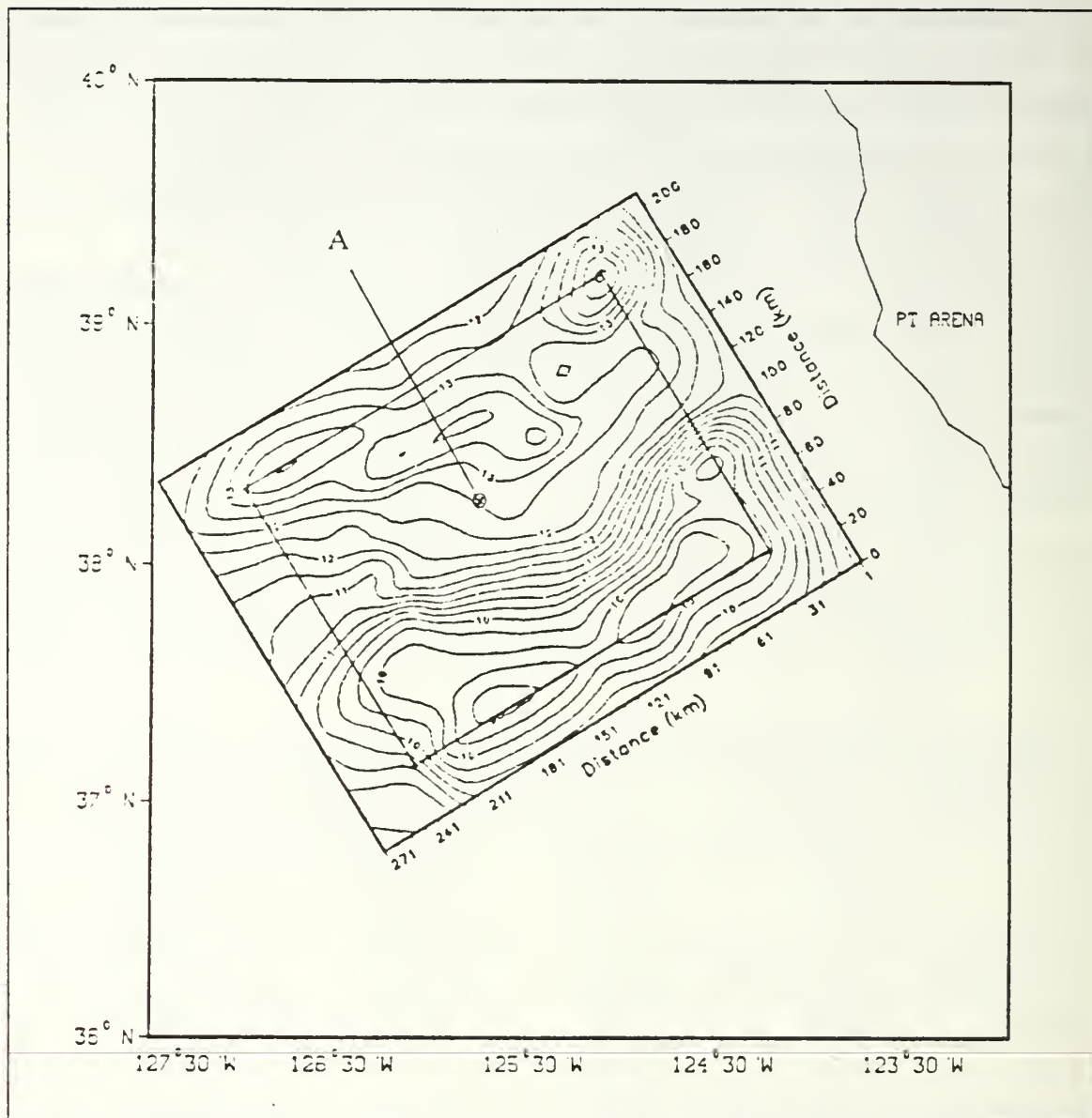


Figure 3. Model Domain Temperature at 85-Meter Depth: (Inside frame represents data area) Contour interval is 0.5C.

field in this experiment ranged from 14.4 degrees at the 10-meter level to 2.09 degrees at 3100 meters. The major difference is of course, the anomolous temperatures extending to over 1200 meters. The temperature gradients associated with such anomalies determine the initial velocity fields through the thermal wind relation.



Figure 4 depicts the initial vertical temperature profile in the warm eddy (point A in Figure 3) and the mean temperature profile of the whole domain. The mean temperature profile of the entire domain decreases with depth, from 13.6 C at the 10m level to 2.09 C at 3100m, while the profile taken at point A of Figure 3 is representative of the warm eddy. At 10m the temperature is 14.45 C, and it also decreases with depth to 2.09 C at 3100m, but the warmer temperatures persist to 1200m or deeper. Figure 5 displays this more clearly, with the upper 40m being a full degree or more warmer than the mean and the difference at 1200m only about 0.3 C. These figures show that the vertical extrapolation procedure was effective in spreading the temperature fields (means and anomalies) with depth. In the future, more sophisticated methods such as dynamical or empirical modes may be used for this purpose. These two figures clearly demonstrate the striking differences between using a climatological temperature profile as an initial condition, and an actual temperature field.



TEMPERATURE PROFILE  
warm eddy vs mean temp profile

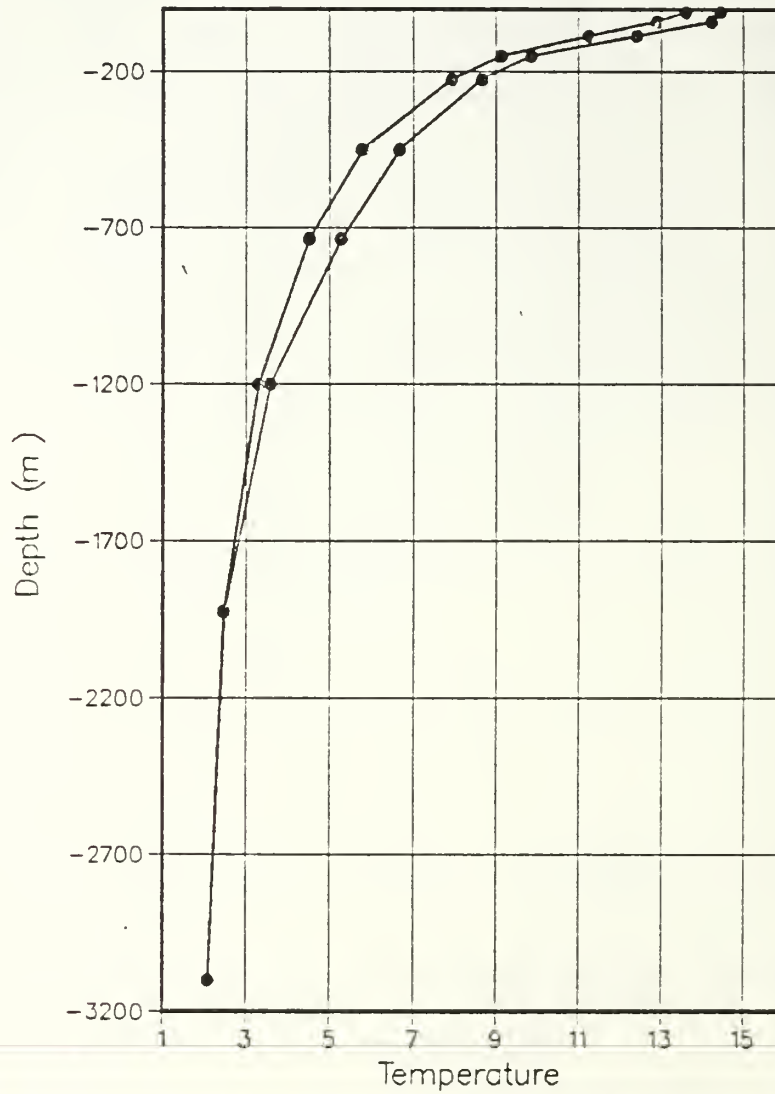


Figure 4. Temperature Profile: Warm eddy (Point A) vs Mean profile for entire domain

TEMPERATURE PROFILE  
temp anomaly in warm eddy

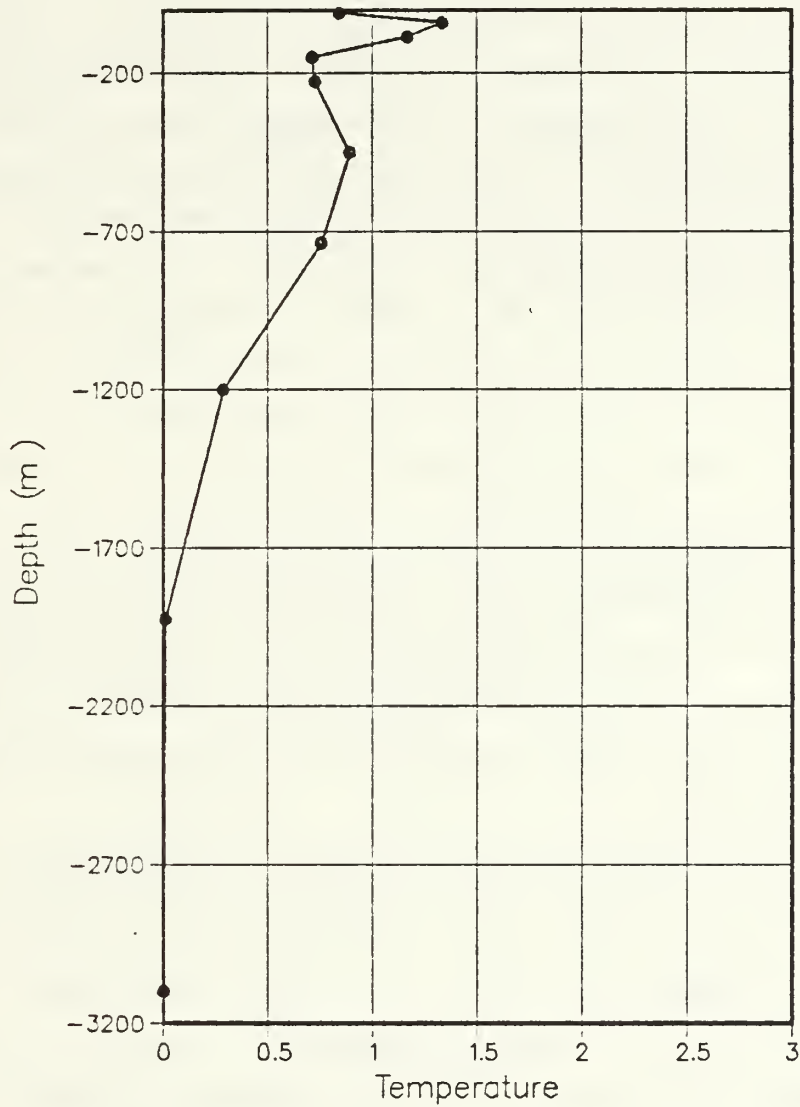


Figure 5. Temperature difference between warm anomaly and mean, (Point A): (Zero represents mean temperature at each level)

### III. MODEL RESULTS

#### A. INITIAL TEMPERATURE, CURRENT AND PRESSURE FIELDS

The quasi-synoptic temperature field of 30 June-5 July has a central date of 3 July which is considered to be day 0, or the initial start time for this model simulation. Day 6 then corresponds to 9 July and day 14, to 17 July. Figure 6 shows the horizontal temperature fields at day 0 at depths of 10, 85, 150 and 225 meters. While each level clearly shows its own distinct thermal signature, there is considerable vertical continuity as well. At each level a warm mass or wedge in the north-central portion of the domain is in contact with a colder section in the southern portion of the domain, producing a gradient, or thermal front, between the two masses. The time evolution of this gradient will be described in detail in Section III.B since it is readily identifiable and since it is ultimately responsible for the strong initial currents in the upper ocean. These currents, computed from the thermal wind relation and the assumption that the vertically averaged current is zero, are depicted in Figure 7 at the 10-meter level. The solid contours represent onshore zonal velocity and poleward alongshore velocity. The strong offshore jet in the center of the domain has typical speeds greater than 40 cm/sec with a maximum value of just over 70 cm/sec. Rienecker *et al.* (1987) also found offshore velocities of 60 cm/sec in the same region. The alongshore currents, southward in the eastern part of the domain and northward in the western part, are somewhat weaker with maximum magnitudes near 40 cm/sec.

The actual flow is the resultant of the two velocity components and is more readily inferred from the bottom diagram in Figure 7, which shows the perturbation pressure field (dynamic height in centimeters) of the top level in the model relative to 2400m. In the diagnostic computation and display of dynamic height fields, 2400m represents the level of no motion, and will be discussed in Section III.C. The solid contouring in the northern part of the domain in this "P" diagram is indicative of a warm high pressure center with associated anticyclonic flow. The dashed contours in the lower half represent lower pressure and thus, cyclonic flow around the low centers. This depiction clearly reveals what happens to produce a "squirt", or offshore jet. The anticyclone and cyclone combine to act as a "nozzle", accelerating the water seaward at high velocities. The "U" diagram shows the strongest offshore speeds in the center of the domain, which corresponds to the area of strongest gradient on the "P" diagram, between the two

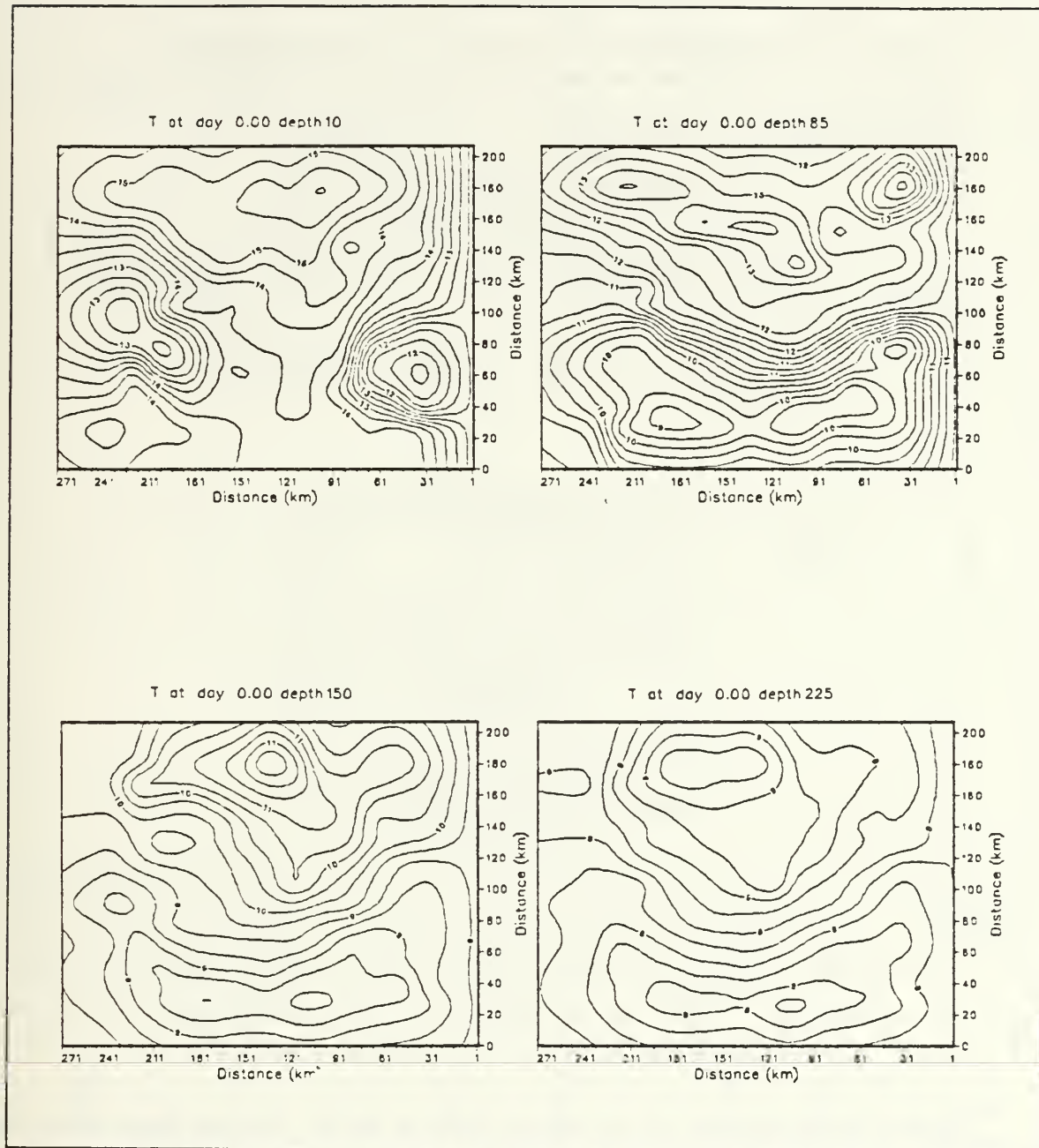


Figure 6. Input temperature fields at 10, 85, 150 and 225 meters: contour interval(ci)=0.5 C.

pressure centers. In contrast, the maximum onshore velocity is only 40 cm/sec, and that is generated in the southern border region which was imposed by the assumed damping of the temperature anomalies toward the boundaries.

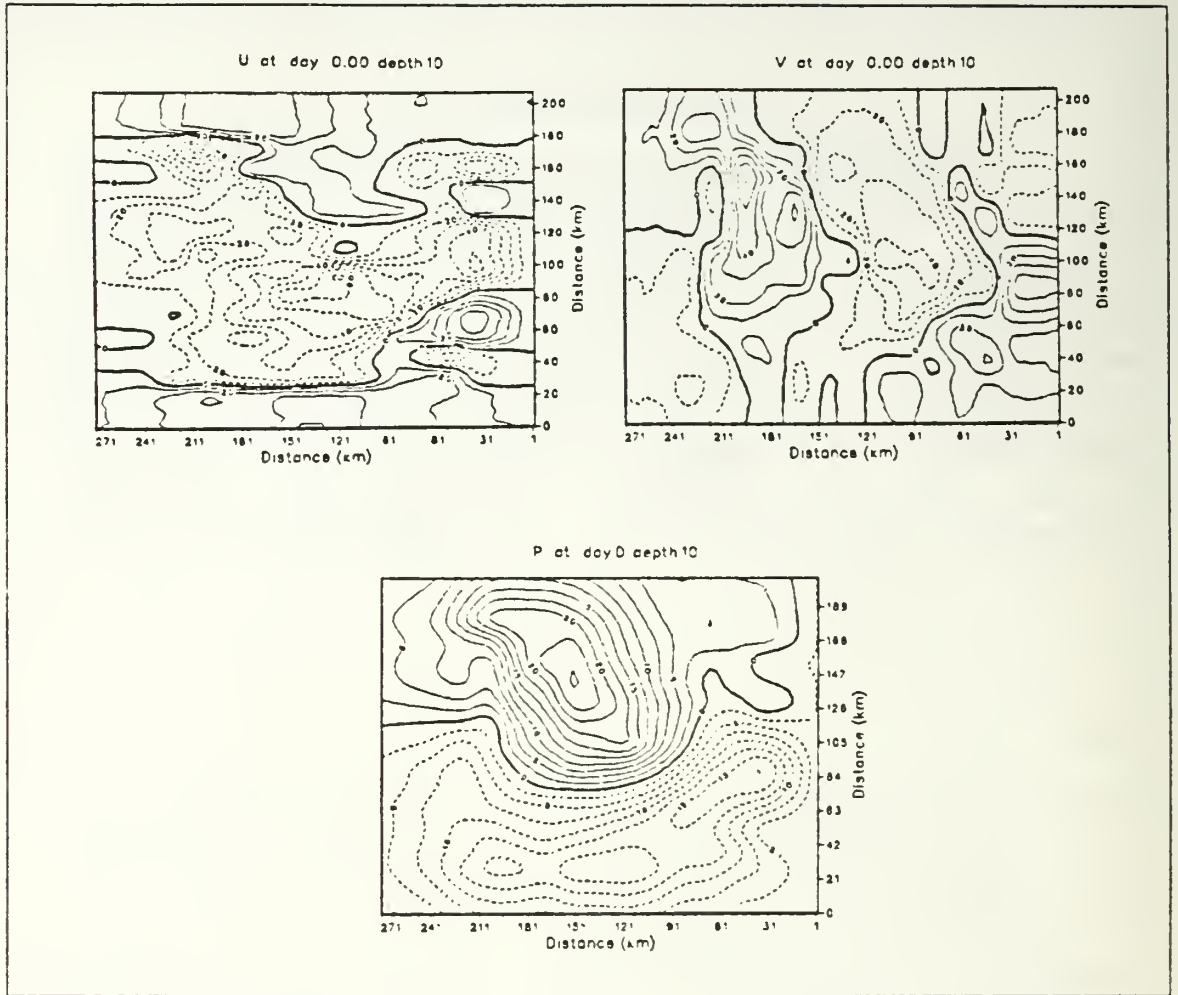
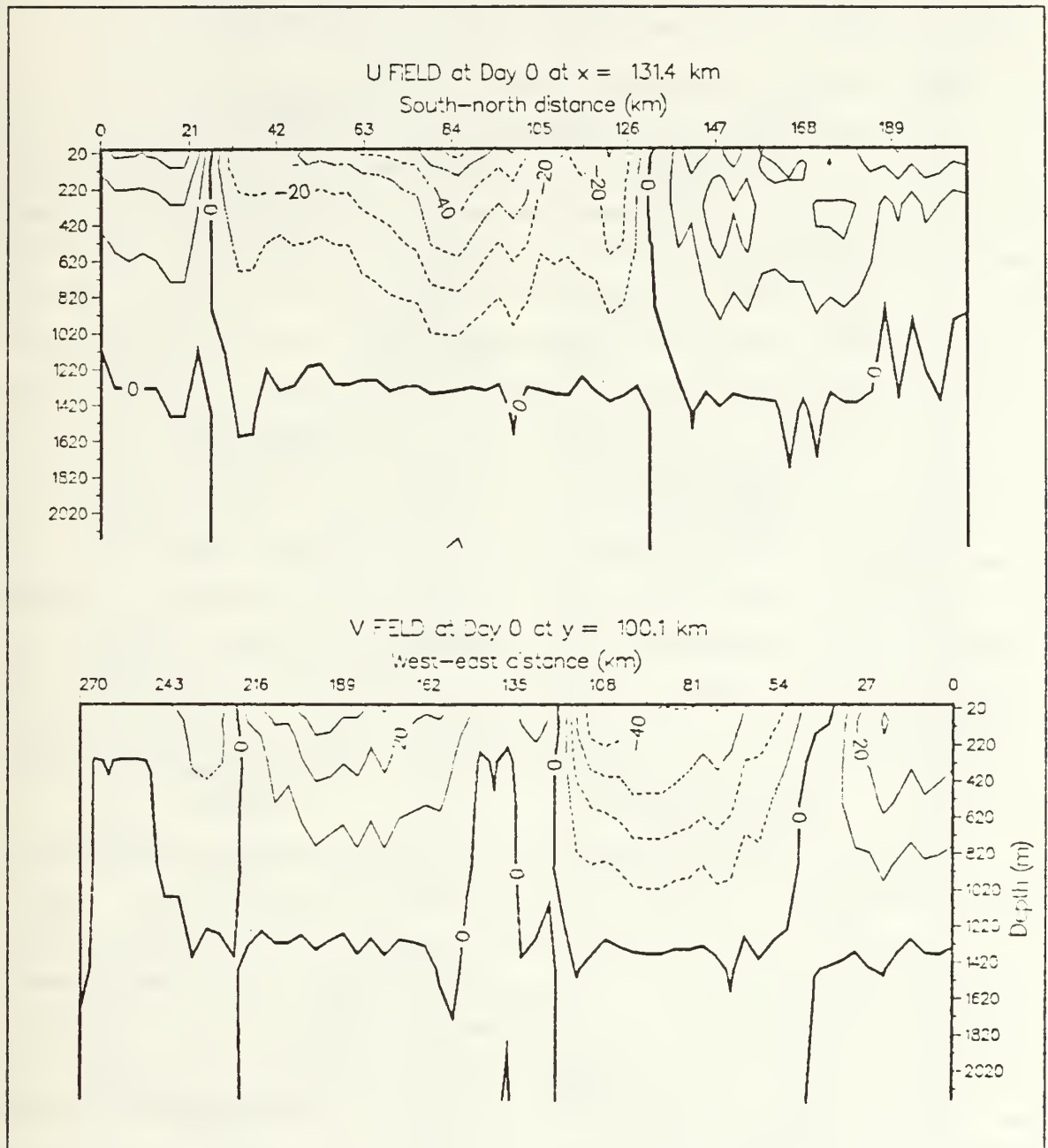


Figure 7. U,V & P, at 10-meters, Day 0: (Top left, Shoreward velocity; Top right, Alongshore velocity,  $c_i = 10 \text{ cm sec}$ , solid contours represent onshore and poleward velocities; Perturbation Pressure,  $c_i = 2.5 \text{ cm}$ , solid contours represent high pressure)

Figure 8 shows sections of the velocity fields at day 0. The top figure shows the shoreward (U) velocity field in a north-south section through the center of the high pressure area while the bottom represents the alongshore (V) velocity, in a zonal section approximately halfway through the domain. The solid contours represent onshore flow ( $U > 0$ ) in the top diagram and poleward flow ( $V > 0$ ) in the bottom diagram. Taken together the two sections show the large-scale current patterns in the upper 2km of the model. These include the strong offshore jet ( $U < 0$ ) near  $y = 84 \text{ km}$  with weaker onshore



flow ( $U > 0$ ) both to the north and south of the jet. It can be seen that the large-scale currents associated with the initial temperature fields are significant primarily in the upper 1000m.



**Figure 8.** Sections of Shoreward( $U$ ) and Alongshore( $V$ ) Velocity, Day 0: Taken through near center of domain, ( $c_i = 10\text{cm/sec}$ ). (Depth scale shortened for easier comparison)

The above "snapshot" of the fields at day 0 (3 July) depicts the velocities and flow patterns produced solely by the temperature input and the PE (geostrophic) computation in the model, at *initialization*. What follows is an examination of the evolution of these features with time, as observed and as predicted by the PE model.

## B. TIME EVOLUTION OF THE FIELDS

A good overview of the time development of the flow field predicted by the PE model for the two weeks following the initial time is seen in the near surface temperature field (Figure 9). The thermal signature present in the main upper ocean front is distinct enough to recognize from day to day, so its movement can be easily seen. The 85m level is the best level to use for this purpose because of the strength of the gradient, although a strong gradient is also present at deeper depths (450m). In the center of the domain, this thermal gradient moved southward about 25-30 km in the first four days, indicating a translation speed of 6-7 cm/sec for the front. What is even more evident is the intensification of the gradient, i.e., from an initial 2-degree change in 30 km, the gradient has tightened to 2 degrees in 15 km, or doubled in intensity. The portion of the front nearer the coast has pushed northward about 80 km in the first 6 days, while the rest of the front has moved south and west, stretching and thus, tightening the gradient. During this two-week period that the front intensified, small mesoscale features or warm cells were seen on the warm side of the front traveling from the northeast part of the domain southwestward, then northwestward along the front. At the same time the cold water to the south of the front pushed eastward and then northeastward, reorienting the front in a more north-south direction.

A comparison of the time evolution of the perturbation pressure at 85m (left column of frames) with that at 225m (right column) is shown in Figure 10 from day 0 to day 14. At 85m, day 0, the dynamic height is a maximum of 22.5 cm in the center of the high pressure area, and a minimum of -15 cm at the center of the low near the eastern boundary. The total difference is 37.5 cm, while the 225m-level range is from 17.5 to -12.5 cm, or a 30-cm difference. By day 14, the difference has increased slightly to 40 cm at 85m and 32.5 cm at 225m, both increases due to an intensification of the low pressure center.

In those two weeks, the center of the warm high pressure at the 85m level moved 60 km to the south while the axis of the jet between the warm high and the cold low has "backed" from westward to southwestward, paralleling the coast. This is due to a northward migration of the low center relative to the high center, keeping the "jet"

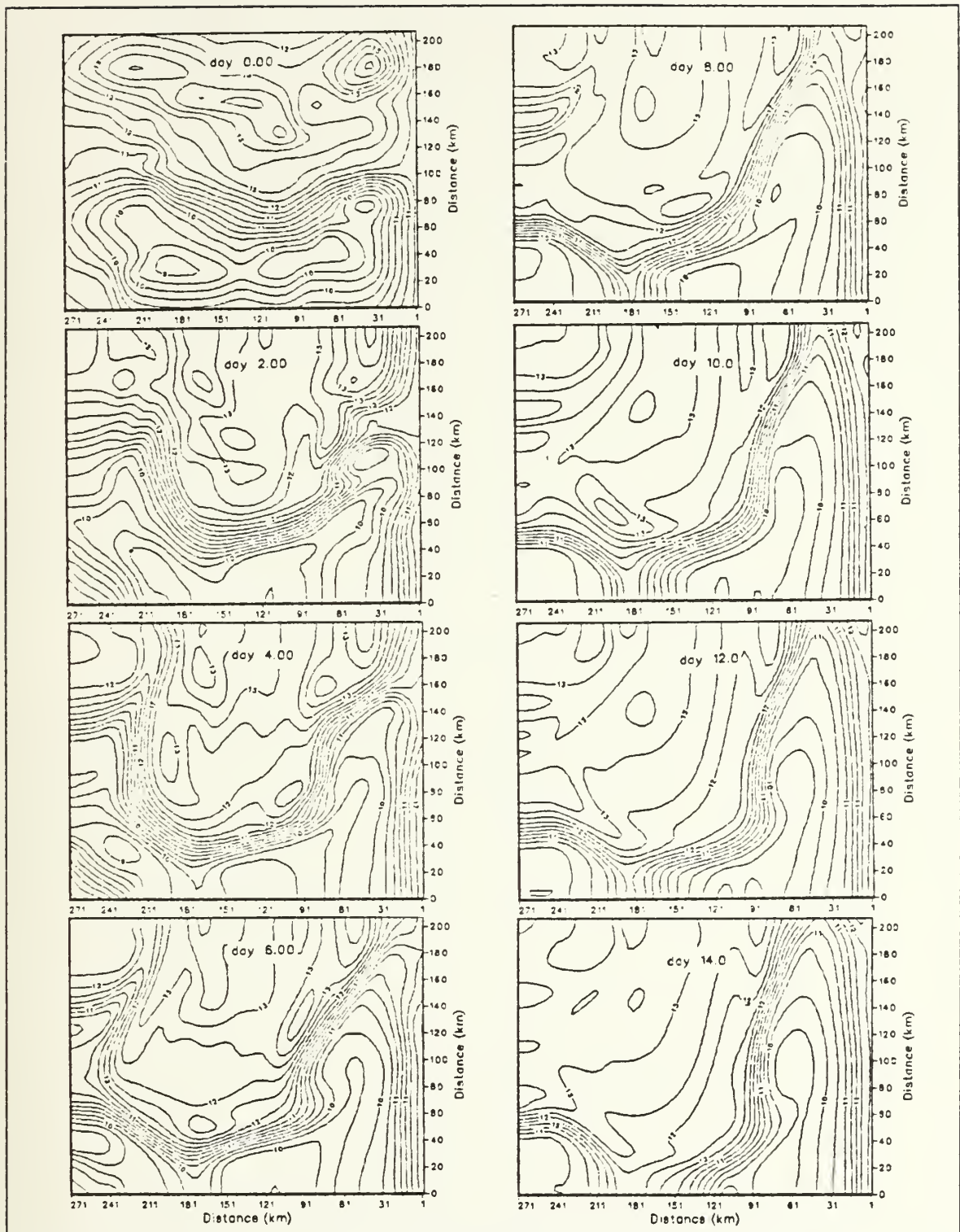


Figure 9. 85m Temperature front, days 0-14(two-day intervals,  $c_i = .5$  C)







between them. Consequently, the zonal component of the jet is weakening at day 14, while the meridional component is strengthening. The 225m level dynamic height field is less intense but the pattern is very similar to the upper levels. The southward displacement of the jet is about 5 km less, suggesting a north-south tilt with depth. This can be seen also in Figure 11, which shows the north-south section of the U-field and the east-west section of the V-field, both taken at day 5. Figure 12 shows the same velocity sections, only at day 14. It can be seen that at day 5, the westward zonal jet is located further south at the surface than at 800m depth. Thus, the jet is tilting towards the warm water with increasing depth. Such a tilt is *suggestive* of baroclinic instability, but a thorough analysis of the actual energy conversions is required to investigate this possibility. Regardless of the mechanism, the PE model predicts a strong development of the thermal field and associated currents during the two weeks following initialization. According to the model, the cold low pressure system located south of the main jet intensifies and moves east-northeastward, reorienting the jet to a more north-south direction.

### C. VERIFICATION/COMPARISON WITH QG MODEL

#### 1. Domain and Initialization

Before making comparisons with Rienecker *et al.* (1987), the domains of each model run must be matched geographically in order to have meaningful comparisons. Figure 13 shows the data domain used in this paper (solid lines) and the domain used by Rienecker *et al.* (1987) (dashed lines). (See also Figures 1,2 and 3 of this paper.) Those authors used data from OPTOMA11 to initialize a 150km square domain for their QG model while the PE model used a rectangular domain, including all of the data out to longitude 127.02W. These dimensions do not include the border regions of either model.

Figure 14 shows this relationship of orientation on the sea surface temperature(SST) and surface dynamic height(SDH) at initialization. Figures 14a and 14c are adapted from Figure 3 of Rienecker *et al.*(1987). Figure 14a depicts a sea surface temperature map made by objective analysis using data from two cruises of OPTOMA11, covering an asynoptic time frame of 23 June to 10 July, 1984. The framed area represents the data domain of the PE model, which used data taken 30 June to 5 July, 1984, OPTOMA11, Leg DII only, for a quasi-synoptic picture. Figure 14b shows that same area, with the temperature contours done initially by subjective analysis and



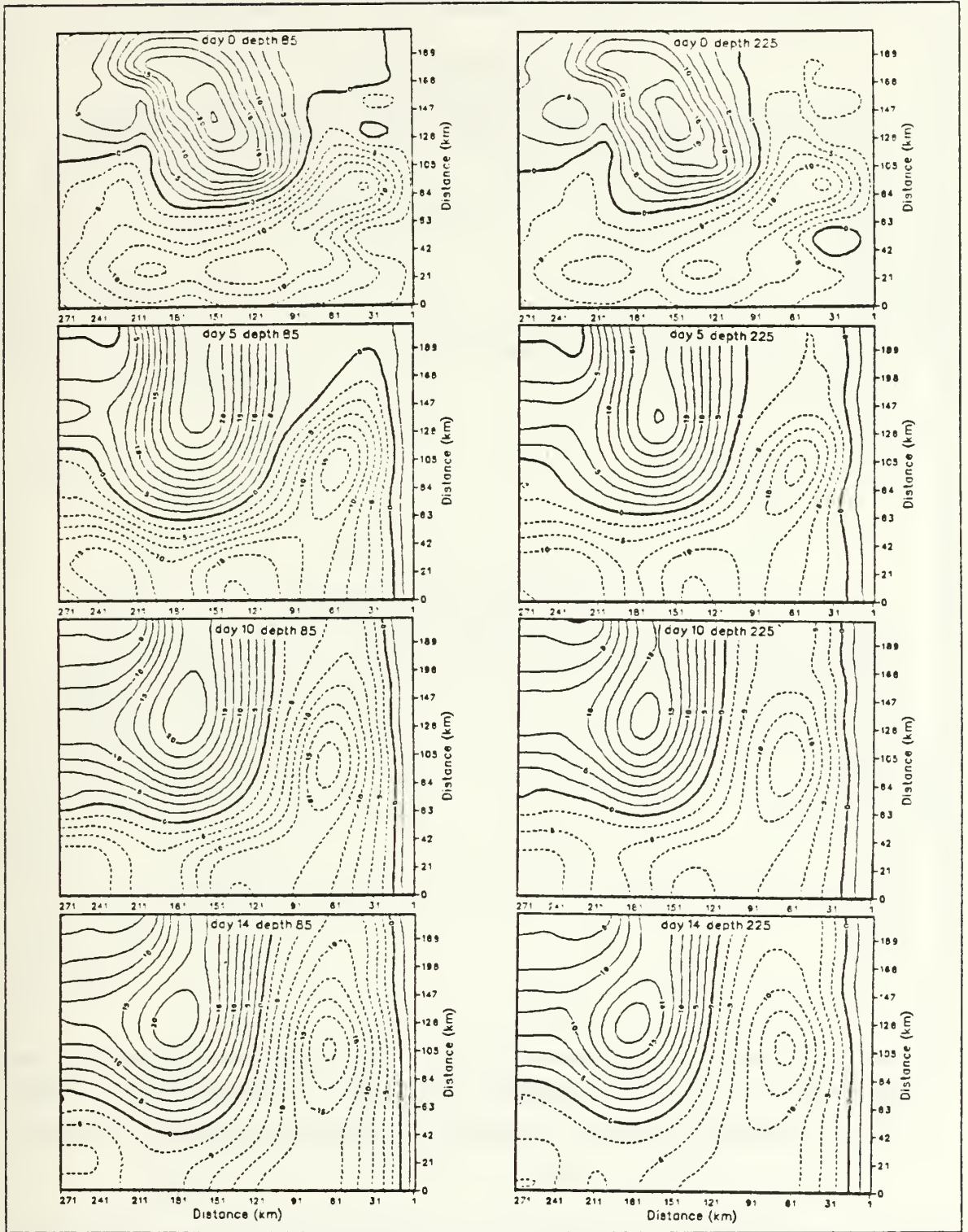


Figure 10. 85m and 225m P-field evolution days 0, 5, 10 and 14 (ci = 2.5 cm)

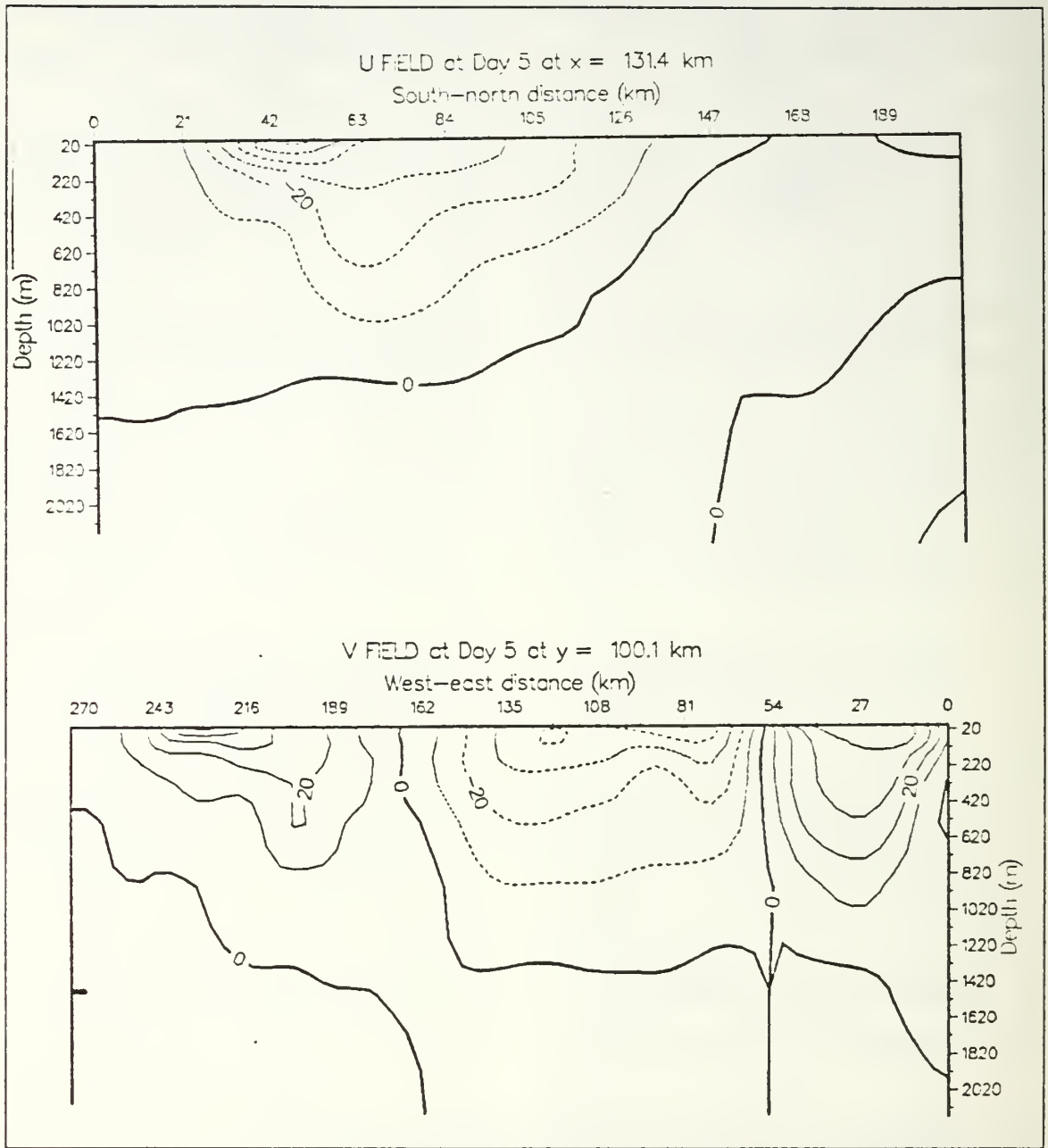


Figure 11. Sections of Shoreward(U) and Alongshore(V) Velocity, Day 5: Taken through near center of domain, ( $c_i = 10\text{cm/sec}$ ). (Depth scale shortened for easier comparison)

plotted for the 10m level. The similarity in the patterns is evident even though separated by 10 meters and prepared by different techniques.

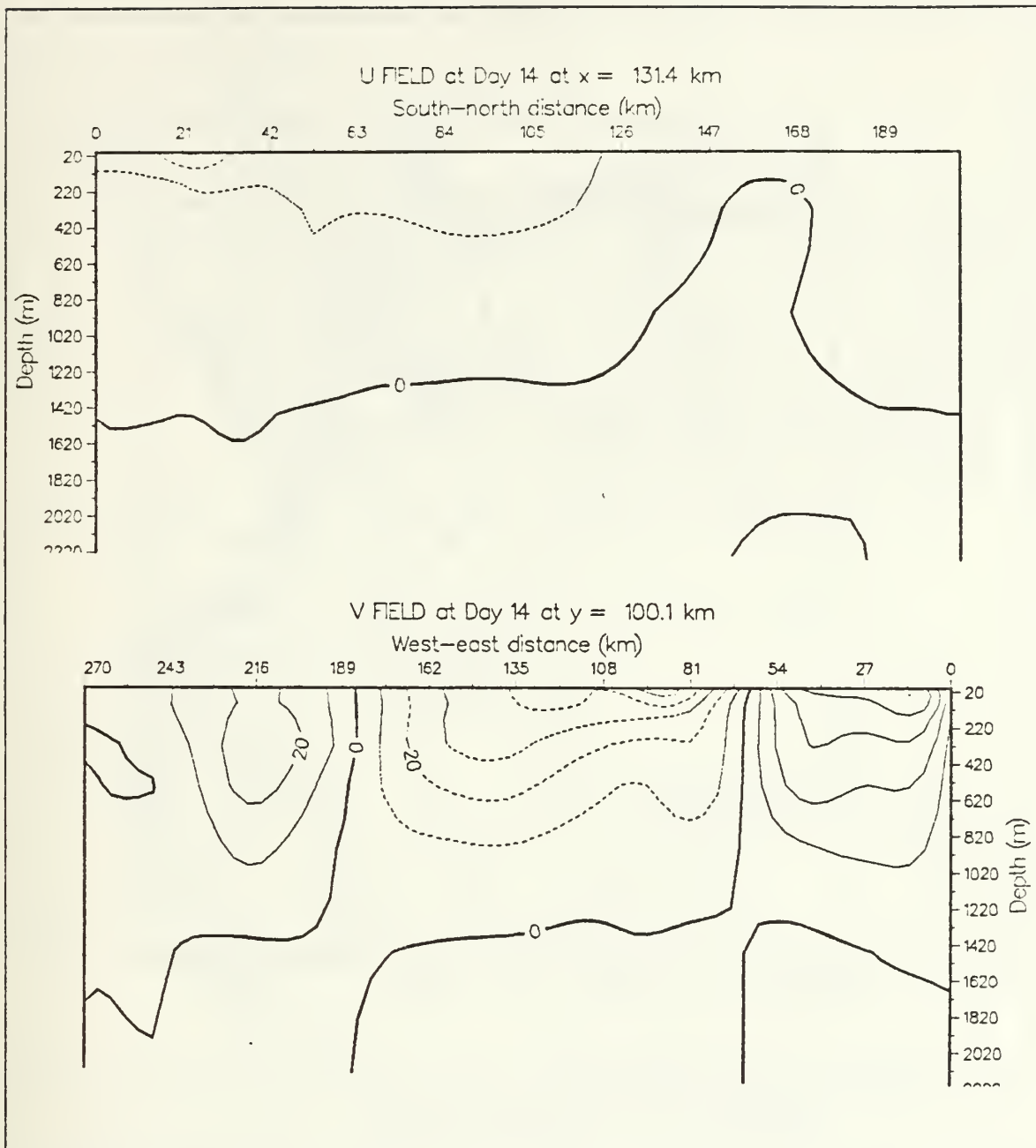


Figure 12. Sections of Shoreward and Alongshore Velocity, Day 14: Taken through near center of domain, ( $c_i = 10\text{cm/sec}$ ). (Depth scale shortened for easier comparison)

Figure 14c depicts the surface dynamic height(SDH) relative to 450m, with the asynoptic time frame as in Figure 14a, as computed from observations by objective

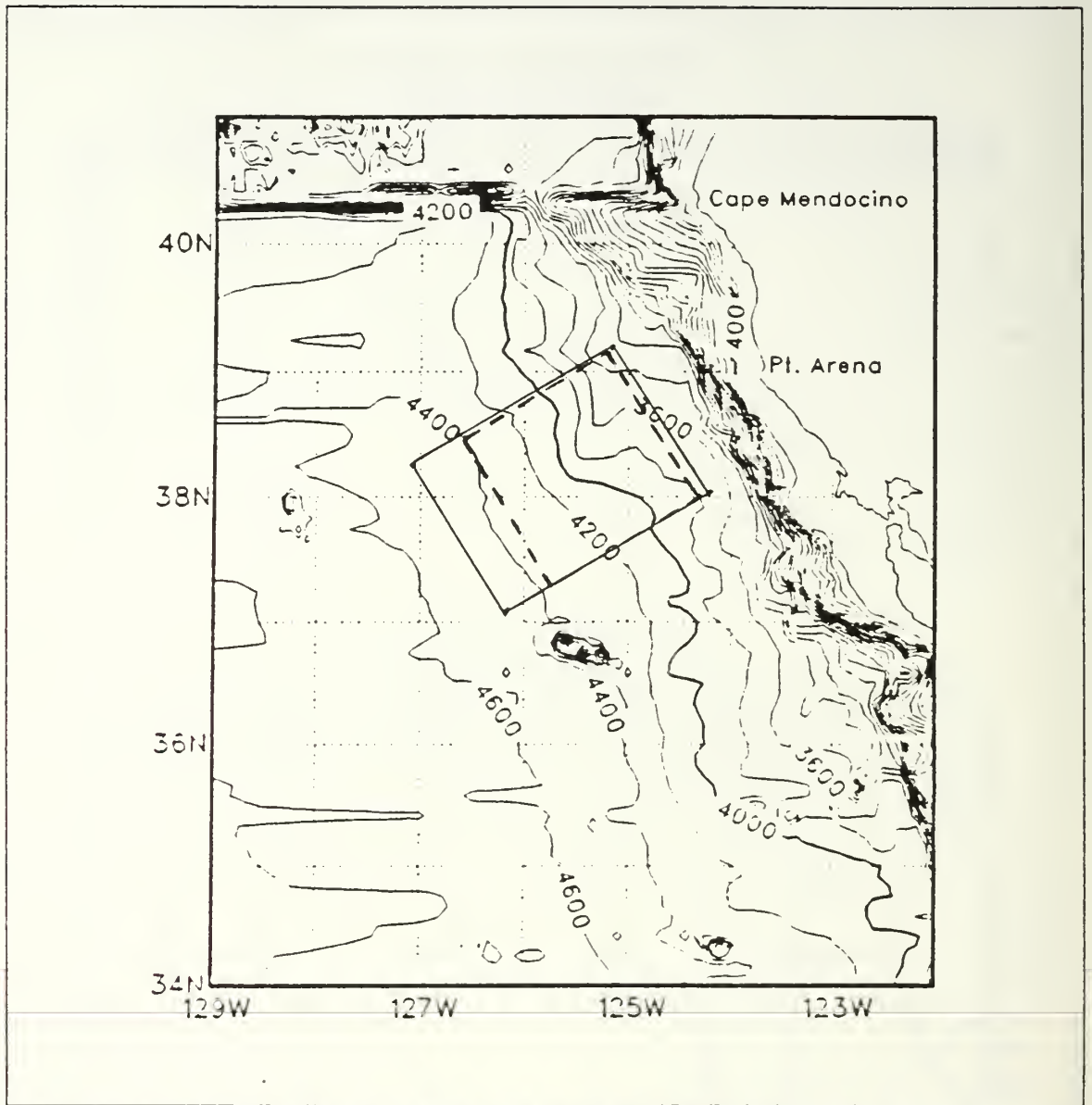


Figure 13. Model Domains(PE = solid, QG = dashed)

analysis. Figure 14d shows the perturbation pressure at 10 meters relative to 450m computed from the PE model. Again, the similar patterns are evident despite the slight differences in synopticity of input data. These figures provide evidence that both the QG and the PE models were initialized with essentially the same data; therefore the results of each should be a good comparison of the dynamics involved, despite the slight differences in synopticity.

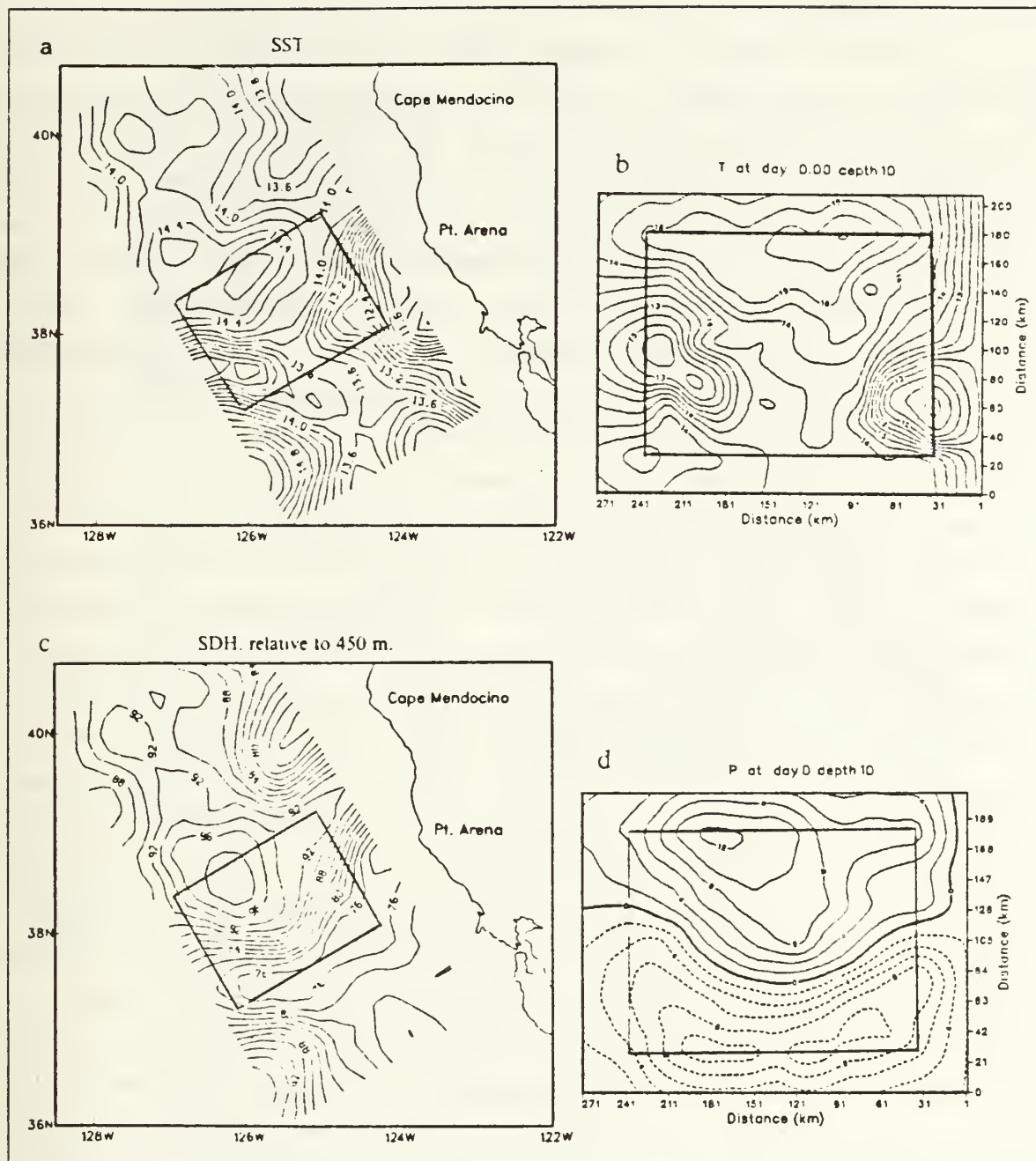


Figure 14. Initial Temperature field and Dynamic Height: (a) Sea Surface Temperature (SST) from Rienecker *et al* ( $ci=0.2$  C); (b) Temperature at 10m from PE ( $ci=0.5$ ); (c) Surface Dynamic Height (SDH) from Rienecker *et al*. ( $ci=2$  dyn cm); (d) 10m P-field from PE ( $ci=2$  cm) (Boxed-in sections represent equivalent areas)



## 2. Verification

Rienecker *et al.* (1987) constructed SDH for each of the six legs or cruises from OPTOMA11 (total time span 5 June to 5 August, 1984) to compare with the QG model runs. Three of these will be borrowed from their Figure 5 for use in this paper. Figure 15a depicts the observed SDH from Leg AIII, 5-13 July, which corresponds to day 6 of the PE model run. This field was computed by objective analysis, Rienecker *et al.* (1987). Figure 15b shows the PE model-predicted surface P-field relative to 450m of day 6 as a comparison. Figure 15c shows the 50m (non-dimensional) dynamic streamfunction, relative to 750m, as predicted for day 6 (their day 193) by the QG model of Rienecker *et al.* (1987) using wind stress curl forcing estimated from FNOC wind analyses. Figure 15d shows the P-field at 50m, also relative to 750m, predicted for day 6 by the PE model of this paper. The inset squares on the two right-hand figures represent the area of the PE model domain that corresponds to the 150km sq area of the observed and QG model prediction of the left figures. On both PE figures, the center of the high pressure is in the upper left corner of the inset box, which matches fairly well with the actual location of the high on Figure 15a, but the center of the low pressure area is about 30km east of the actual position on the verification panel. This difference in position of the cyclonic center effectively removes the "crimp" out of the "jet" that is so apparent in Figure 15a, and consequently the PE pressure gradient runs diagonally rather than zonally. Figure 15c, the QG-predicted streamfunction at 50m, shows more of the zonal flow at day 6 than does the PE P-field. The QG-predicted "jet" orientation here is similar to the verification panel, significantly better than the PE pressure field of Figure 15d, but the location and axis of the cyclone-anticyclone pair predicted by the PE pressure field is nearer reality than the QG streamfunction predicts. The SDH verification field, Figure 15a, shows the "jet" between the high and low centers to have moved further offshore than the PE model predicted, and the feature itself distorting into a very tight gradient with an abrupt 90 degree direction change to the south, then another shift back to the west. This offshore motion is not predicted by the PE model because the low pressure center has moved northward further in the model, causing a north-south "jet" axis shift between the high and low centers which eliminates much of the zonal flow.

Figure 16 is the same as Figure 15, except that prediction day 14 rather than 6 is shown. The verification SDH in panel "a" is taken from Figure 5 of Rienecker *et al.* (1987), and is based on the data collected on Leg P of OPTOMA11. This is the most



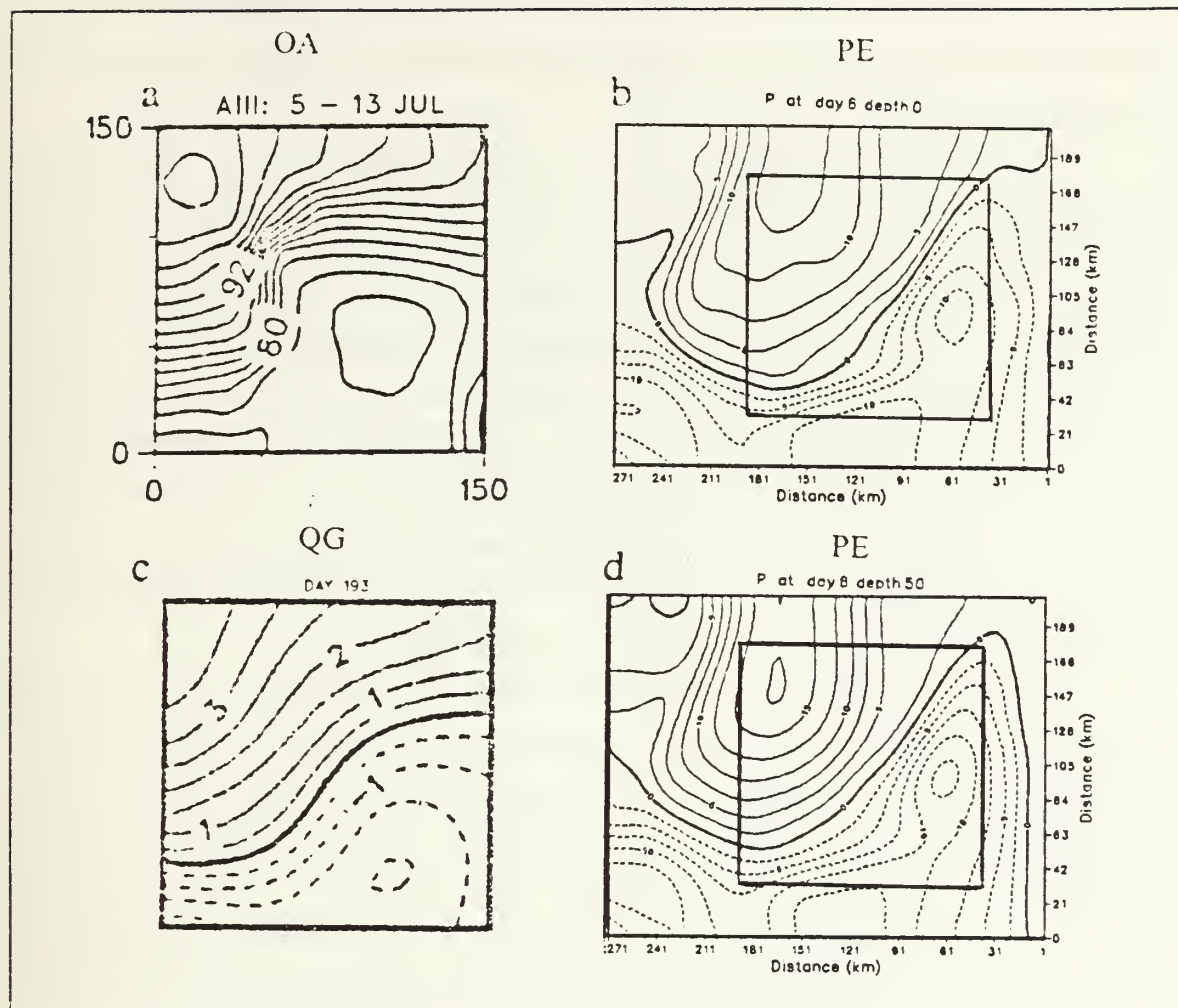


Figure 15. Day 6 Verification and Comparison: (a)SDH, Leg AIII, from Rienecker *et al.* ( $c_i = 2 \text{ dyn cm}$ ); (b)Surface P-Field day-6 PE Prediction ( $c_i = 1 \text{ cm}$ ); (c)QG prediction for day-6 dynamic streamfunction at 50m; (d)50m P-field from PE prediction for day 6 ( $c_i = 2.5 \text{ cm}$ ) (Boxes in right panels correspond to left panel areas)

synoptic data of the program, having been taken by aircraft (P-3) on 18 July, 1984, in about 8 hours. Due to depth limitations of data, a 300m reference level was used to compute the SDH of the verification panel, so the same reference level was used for computing the day 14 surface P-field predicted by the PE model (panel b) for better comparison. (Note that day 14 of the PE prediction is actually 17 July, one day before the verification panel, but the elapsed time of model run is the same for PE and QG,

with one day difference for the start time, so it is used for comparison.) Panels c (QG-predicted streamfunction at 50m) and d (PE predicted  $P'$  at 50m) both use a 750m reference level, however.

The high pressure center is still located in the northwest corner of the inset of the PE prediction panel, but the center of the high in the verification has moved west, out of the panel domain. The low center or cyclone is predicted by the PE model to be about 30km further *south* than the verification shows. (Recall from Figure 15a and b that the day 6 prediction was *north* of the verification). The gradient or "jet" is nearly bisecting the domain meridionally on the prediction, while the verification still shows zonal flow in the northern third of the domain. The intensity of the predicted cyclone in Figure 16b has pulled the gradient tightly in and away from the anticyclone while the verification in Figure 16a shows the gradient to have weakened since day 6. The improvement in synopticity of the later data (8 hours vice 8 days) may have something to do with this apparent weakening of the analyzed gradient.

The QG prediction at 50m, shown in Figure 16c, again was done with wind stress curl forcing added. The gradient runs diagonally through the domain in the general direction of the verification field, northeast to southwest, but without the cyclonic and anticyclonic curvature. The 50m PE prediction is much the same as the surface prediction, with the gradient running basically north-south, but it finishes in the south with the anticyclonic turn displayed by the verification SDH of panel a. It appears that a combination of QG and PE predictions would come closest to the verification on day 14.

### 3. Discussion and Interpretations

Rienecker *et al.* (1987) chose a reference depth of 750m for a level of no motion, upon which to base the dynamic heights calculated and predicted by their QG model. In contrast, the PE model does not assume a particular reference level, but rather assumes that the vertically averaged current is zero. According to the model currents in Figures 11 and 12, this results in an approximate level of no motion near 1200 meters. Figure 17 shows the perturbation pressure field at 450 meters at initialization (day 0) of the PE model, and the resultant U velocity field. The vertical continuity is apparent with the persistence of the cyclonic-anticyclonic features which are seen at shallower levels, still present at 450 meters, albeit in weaker form. The downward extrapolation of the 450-meter temperature anomaly is responsible for this dynamic picture present at this depth, and the dynamic height and, consequently, velocities, could be altered by using

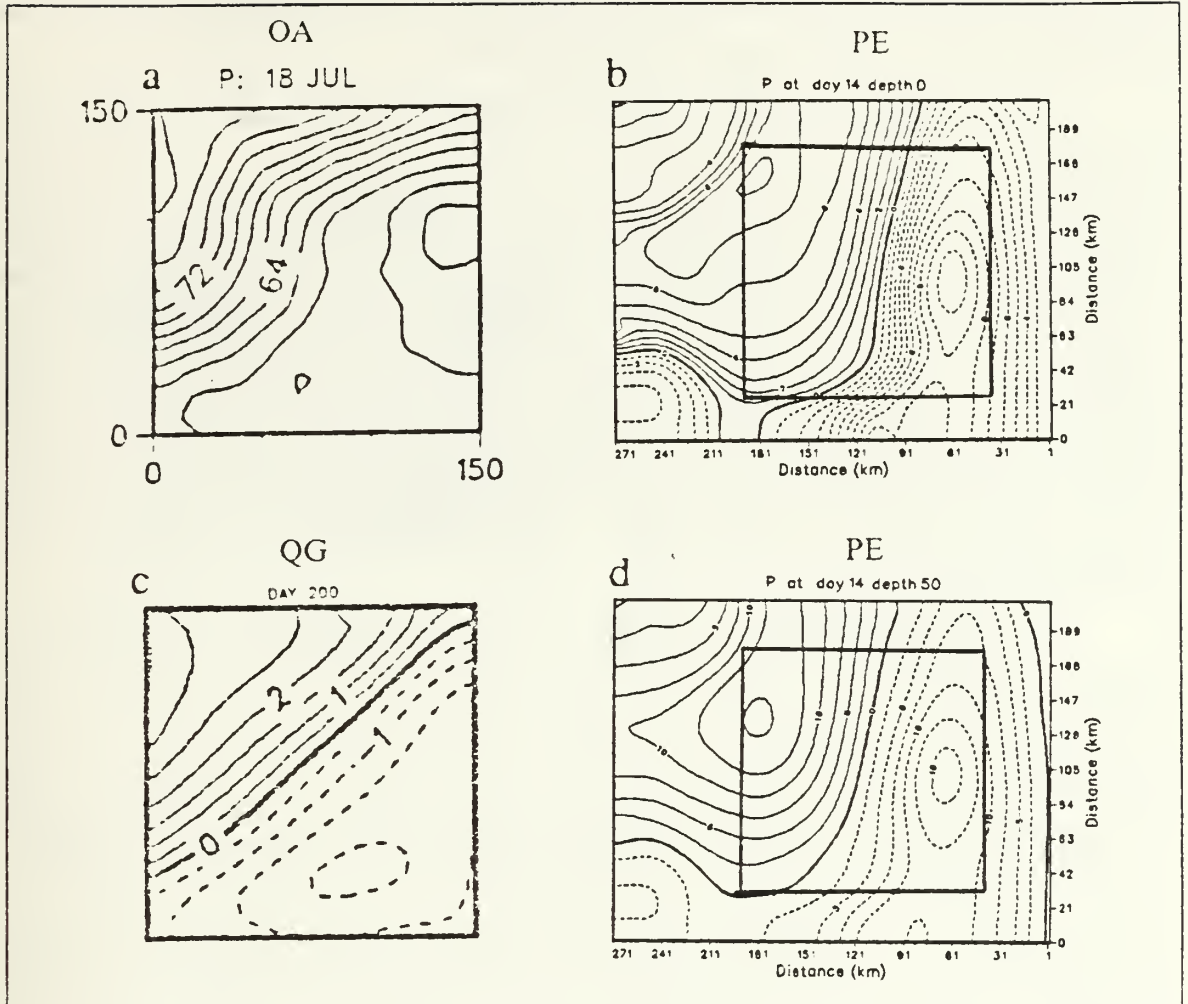


Figure 16. Day 14 Verification and Comparison: (a)SDII. Leg P, from Rienecker *et al.* ( $c_i=2$  dyn cm); (b)Surface P-Field day-14 PE Prediction ( $c_i=1$ cm); (c)QG prediction for day-14 dynamic streamfunction at 50m; (d)50m P-field from PE prediction for day 14( $c_i=2.5$  cm) (Boxes in right panels correspond to left panel areas)

different vertical extrapolation techniques. Figures 4 and 5 show a warm-anomaly of nearly one degree at 450m, however, and to terminate this anomaly abruptly, which is really closer to two degrees total differential across the front, does not seem to be a physically correct procedure. Without observations below 450m, it is not possible to know what the real temperature anomalies at great depths are in any given case. Whether any of the differences between the QG and the PE model results can be

attributed to this difference in level of no motion cannot be determined without further sensitivity studies, as will be discussed in Section IV.B.

For the initial conditions used in this study, the PE model was sensitive to changes in the open boundary conditions, and several variations were tried unsuccessfully before a satisfactory condition was found. Virtually all the conditions chosen except the one that worked became unstable very quickly, in two or three days model run time, and produced poleward coastal jets of 500 cm/sec or more. Appendix B lists the open boundary conditions tried in detail, since this paper is not a study of open boundary conditions. Without further sensitivity tests it is not possible to know whether one of the open boundary condition formulations is unstable (unlikely) or whether the linear computational stability condition ( $c \frac{\Delta t}{\Delta x} < 1$ ) was violated by the jet, or whether some other instability occurred.

The isothermal condition imposed at each model level along the coastline resulted in varying degrees of slope of the isotherms between the boundary of the data field and the coastline. These slopes produced thermal wind inflow from both the north and from the south (e.g., Figure 3). Since the slope of the isotherm in the south was greater than in the north, inflow from the southern boundary tended to dominate in this border region, simulating an intense poleward coastal jet that was subsequently predicted to intensify with time. A different procedure at the eastern boundary would have produced a varying amount of flow from the south or from the north in the border region, resulting in a different model initial condition and perhaps a different model prediction. Another method of treating the eastern boundary is to "open" it, like the other boundaries, with no coastline. The robustness of the model results to the open boundary conditions and to the method of extrapolating the data to the various model boundaries needs to be examined further, as discussed in Section IV.B.



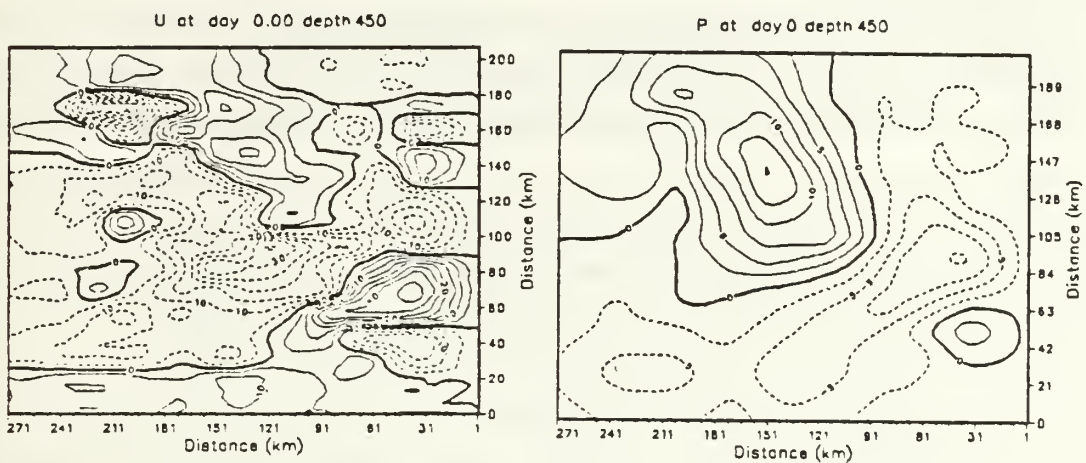


Figure 17. Pressure and Zonal velocities, Day 0, 450m (ci = 2.5cm, 5cm/sec)

## IV. SUMMARY AND RECOMMENDATIONS

### A. SUMMARY

This PE model run utilized observed temperature data gathered by Leg DII of OPTOMA11, 30 June-10 July, 1984 as initialization for the purpose of predicting thermal feature movement in the California coastal region. The specific area of coverage, a 31,000 square kilometer domain 180 km off of Point Arena, was sampled in intervals conducive to verification of model predictions, and Leg AIII, 5-13 July, and Leg P of 18 July were used as verification of the PE model predictions of days 6 and 14. Rienecker *et al.* (1987) also used OPTOMA11 in the same manner for the initialization of their QG model, so their results were used extensively for comparison as well.

The observed initial offshore jet velocities of 60 cm/sec or more in the PE model echo the findings of Rienecker *et al.* (1987), whose model produced similar surface jets. These jets were verified by satellite images that clearly showed at least the presence of jets and meanders, if not the velocities. The input surface temperature fields and surface dynamic height and pressure surfaces of each model were matched with objective analysis-calculated verification panels and found to be basically equivalent at the outset of model simulations. The differences between the two models at initialization were reference level differences and model domain differences, all of which were accounted for in the comparisons. The QG model's dynamic streamfunction at 50m was compared with the pressure perturbation of the PE model at 50m. Both models were close to verification, even though the QG model was driven by observed winds and the PE model was unforced. For example, both models were within a few kilometers on the 6-day prediction of the anticyclone, but the QG prediction of the cyclone was 40-50km southwest while the PE model put the cyclone 30km northeast of the verified position. Consequently, the jet axis formed by the gradient between the cyclone/anticyclone pair was shifted accordingly. Therefore, by day 6, axis angles between the cyclonic and anticyclonic centers were different between the two models which resulted from translational differences in the dynamic features, with the QG model predicting offshore movement while the PE model predicted southward and northward motion of frontal features.

By day 14, the QG model 50m streamfunction represented the jet basically diagonally across the domain while the PE model showed a nearly north-south



orientation of the jet. The verification SDH of Leg P of 18 July showed mostly offshore flow in the northeast quadrant of the domain, shifting cyclonically to southward flow in the central portion, and turning anticyclonically back to offshore in the southwest quadrant. Based on these results and those from the time series of the 85m temperature field, it is feasible that frontal movement in the California coastal region can be anticipated and, with more sensitivity and case studies (below), could be predicted by a multi-level, high resolution PE model, given synoptic data for initialization.

## **B. RECOMMENDATIONS**

This study represents but one simulation (hindcast) of a single synoptic case in the coastal ocean using a PE model. An important question that needs to be investigated further is how robust the simulated eddy evolution is to various modeling and data processing assumptions. For example, one would like to know how sensitive the simulated results are to the procedures used to extrapolate temperature data into the regions (borders, deep ocean) of no data. The eastern boundary is especially important in this particular synoptic case because there is a strong jet entering the domain from the shoreward edge of the data region. Where did this jet actually come from? Did it come down the coast from the north and turn anticyclonically into the data area or did it come up from the south and turn cyclonically into the region? The method of extrapolating the data toward the lateral boundaries, with particular attention to the eastern boundary, needs to be examined carefully and the sensitivity of the simulation to these procedures needs to be thoroughly investigated. The sensitivity of the model predictions to the method of vertically extrapolating the fields to the deep ocean should also be studied. Alternative methods of vertical extrapolation, such as fitting the anomalies to dynamical or empirical modes, should certainly be investigated.

Another important question to address is what are the dynamical mechanisms that are responsible for the evolution of the eddy fields in this synoptic case. In order to investigate these mechanisms, a number of sensitivity studies and analyses should be carried out. An analysis of the energy and vorticity budgets would be useful to determine the relative importance of purely kinematic effects (horizontal redistribution of absolute vorticity) versus baroclinic development. The sensitivity of these various dynamical effects to the particular data processing and modeling procedures should also be studied. Finally the role of wind forcing (important in the QG simulations) and variable bottom topography should also be systematically investigated.

It is therefore recommended that further PE model studies be conducted using observed data for initialization and verification of dynamic numerical predictions. The OPTOMA program is ideal for that purpose since data which were taken in a quasi-synoptic fashion are provided in intervals of 1-2 weeks, or, as in the case of Leg P of OPTOMA11, within eight hours. A PE model could take such data coverage for an operational area and predict the thermal conditions 1-2 weeks later, which would be a valuable planning tool for the conduct of Naval exercises.

# APPENDIX A. OPTOMA11 STATIONS, LEG DII, 30 JUNE-10 JULY 1984

XBT HEADERS:

STA #	DATE	TIME	LAT	LONG	NPTS
1	84183	113	36.47	-122.10	684
2	84183	200	36.53	-122.21	684
3	84183	300	36.59	-122.31	441
4	84183	407	37.04	-122.41	682
5	84183	503	37.09	-122.50	682
6	84183	603	37.15	-122.58	684
7	84183	700	37.21	-123.06	684
8	84183	815	37.28	-123.17	684
9	84183	906	37.33	-123.25	684
10	84183	1014	37.37	-123.37	652
11	84183	1105	37.42	-123.45	684
12	84183	1243	37.51	-123.59	684
13	84183	1350	37.57	-124.10	684
15	84183	1722	38.09	-124.24	684
16	84183	2036	38.28	-124.38	669
17	84183	2210	38.34	-124.45	668
18	84184	19	38.45	-124.55	684
19	84184	430	38.54	-125.01	684
20	84184	806	39.02	-125.04	684
21	84184	1106	39.09	-125.11	516
22	84184	1705	39.02	-125.19	684
23	84184	1800	38.52	-125.21	684
24	84184	1850	38.43	-125.23	684
25	84184	1957	38.32	-125.27	684
26	84184	2022	38.28	-125.28	671
27	84184	2102	38.20	-125.28	684
28	84184	2139	38.15	-125.28	684
30	84184	2344	38.00	-125.36	684
31	84185	228	37.30	-125.43	684
33	84185	700	37.30	-125.21	667
34	84185	800	37.35	-125.13	684
35	84185	900	37.40	-125.04	684
36	84185	1000	37.46	-124.52	684
37	84185	1122	37.51	-124.40	684
38	84185	1206	37.57	-124.28	684
40	84185	1444	38.03	-124.30	684
41	84185	1544	38.03	-124.44	680
42	84185	1636	38.05	-124.59	684
43	84185	1722	38.05	-125.08	684
44	84185	1810	38.07	-125.21	684
46	84185	2158	38.14	-125.54	684
47	84185	2302	38.18	-126.06	684
48	84186	6	38.22	-126.23	679
49	84186	102	38.25	-126.28	684
51	84186	248	38.31	-126.32	684
52	84186	426	38.38	-126.15	684
53	84186	514	38.43	-126.05	684

54	84186	619	38.49	-125.54	684
55	84186	739	38.55	-125.42	684
56	84186	850	39.00	-125.31	684
57	84186	930	39.03	-125.20	619
59	84186	1226	39.02	-125.10	684
60	84186	1336	38.48	-125.17	667
61	84186	1434	38.38	-125.20	684
62	84186	1534	38.28	-125.24	684
63	84186	1627	38.19	-125.24	684
65	84186	1910	38.13	-125.46	684
66	84186	2000	38.15	-125.56	531
67	84186	2055	38.19	-126.12	684
68	84186	2135	38.21	-126.17	684
69	84186	2230	38.25	-126.28	684
71	84187	44	38.25	-126.49	684
72	84187	138	38.18	-126.58	684
73	84187	221	38.14	-127.02	684
74	84187	319	38.13	-126.50	684
75	84187	430	38.10	-126.35	684
76	84188	517	38.08	-126.23	684
77	84187	621	38.05	-126.30	667
78	84187	722	38.01	-126.43	674
80	84187	1021	37.55	-126.38	684
81	84187	1134	37.53	-126.24	684
82	84187	1300	37.52	-126.12	684
83	84187	1346	37.48	-126.20	684
84	84187	1427	37.44	-126.29	684
86	84187	1733	37.38	-126.21	684
87	84187	1816	37.38	-126.11	684
88	84187	1933	37.35	-126.00	684
89	84187	2013	37.32	-126.08	684
90	84187	2058	37.28	-126.15	684
92	84187	2344	37.21	-126.10	684
93	84188	36	37.20	-126.00	684
95	84188	402	37.12	-126.00	684
96	84188	502	37.07	-126.09	684
97	84188	556	37.03	-126.19	684
99	84188	944	36.42	-126.21	684
100	84188	1044	36.32	-126.15	684
102	84188	1328	36.17	-126.06	684
103	84188	1410	36.10	-126.01	684
105	84188	1744	36.08	-125.50	684
106	84188	2025	36.17	-125.44	684
107	84188	2308	36.29	-125.39	684
109	84189	346	36.49	-125.27	684
110	84189	531	36.57	-125.22	297
112	84189	1056	37.13	-125.13	684
114	84189	1436	37.12	-124.59	684
115	84189	1543	37.04	-124.48	684
116	84189	1649	36.56	-124.39	684
117	84189	1755	36.50	-124.31	684
119	84189	2136	36.51	-124.12	442
120	84189	2342	36.60	-124.05	684
121	84190	110	37.09	-124.01	297
123	84190	440	37.10	-123.53	684
124	84190	534	37.01	-123.49	684

125	84190	634	36.49	-123.45	684
126	84190	731	36.41	-123.40	684
127	84190	923	36.50	-123.34	684
128	84190	1057	36.60	-123.30	684
129	84190	555	37.09	-123.24	684
130	84190	1400	37.05	-123.13	684
132	84190	1719	36.56	-122.48	684
133	84190	1814	36.52	-122.37	684
134	84190	1932	36.47	-122.21	684
135	84190	2014	36.45	-122.12	684
136	84191	55	36.52	-122.09	87
137	84191	202	37.00	-122.19	87
139	84191	440	37.04	-122.41	411
140	84191	607	37.05	-122.57	684
143	84191	1921	37.33	-123.18	684
144	84191	2239	37.47	-123.23	684
145	84192	122	37.59	-123.21	116
148	84192	538	37.56	-123.08	116

CTD HEADERS:

STA #	DATE	TIME	LAT	LONG	NPTS
14	84183	1514	38.01	-124.17	151
29	84184	2224	38.10	-125.31	151
32	84185	335	37.20	-125.43	151
39	84185	1313	38.01	-124.16	151
45	84185	1938	38.10	-125.31	151
50	84186	134	38.28	-126.37	151
58	84186	1122	39.09	-125.11	151
64	84186	1716	38.09	-125.32	151
70	84186	2311	38.28	-126.37	151
79	84187	800	37.60	-126.50	151
85	84187	1526	37.40	-126.37	151
91	84187	2139	37.24	-126.24	151
94	84188	144	37.19	-125.46	150
98	84188	721	36.59	-126.33	151
101	84188	1134	36.24	-126.13	151
104	84188	1510	36.00	-125.55	151
108	84189	100	36.39	-125.34	151
111	84189	752	37.05	-125.17	151
113	84189	1300	37.20	-125.11	151
118	84189	1919	36.39	-124.16	151
122	84190	300	37.20	-123.58	181
131	84190	1510	36.60	-123.01	301
138	84190	247	37.02	-122.23	18
141	84191	814	37.09	-123.15	151
142	84191	1314	37.21	-123.16	112
146	84192	318	38.08	-123.21	29
147	84192	411	38.03	-123.15	19
149	84192	710	37.48	-123.00	9



## APPENDIX B. OPEN BOUNDARY CONDITIONS

### A. INTRODUCTION

The eastern boundary of the PE model was closed because it represents the coastal margin. The open boundary conditions in question relate to the northern, southern and western borders of the model domain, but in particular to the southern boundary since strong inflow occurred there, causing rapid progression to instability. The changes to correct the instability problem were made consistently each time, to each boundary (other than the eastern one), but in this description only the southern boundary conditions on the northward velocity ( $V$ ) are described to avoid repetition. To eliminate terminology problems, the following are stated for clarification:

- Superscript "t" refers to time differencing at gridpoints
- subscript "B" refers to space differencing between gridpoints, where "B" represents the open boundary
- "V" is meridional velocity component
- "C" is northward phase speed computed near the southern boundary
- VD is the velocity difference between adjacent gridpoints
- CV is the computed phase speed used to determine inflow or outflow at a boundary, depending on sign ( $< 0$  = outflow,  $> 0$  = inflow)

### B. PROBLEM #1

The initial model run developed a strong surface inflow jet from the south immediately, and went unstable ( $V > 100\text{cm/sec}$ ) by day 4. Even to depths of 735 meters and below, velocities above 300 cm/sec were generated by day 10 of model run time. The boundary conditions on the meridional velocity component at the southern open boundary were determined by first computing the spatial difference,

$$VD = V_{B+2}^{t-1} - V_{B+1}^{t-1}. \quad [7]$$

In the event that  $VD = 0$ , the boundary was set according to

$$V_B^{t+1} = V_{B+1}^{t+1}. \quad [8]$$

If  $VD \neq 0$ , the boundary was set by computing

$$CV = - \frac{\Delta y}{\Delta t} \frac{(V'_{B+1} - V'^{-1}_{B+1})}{VD} \quad [9]$$

so that if  $CV < 0$  (outflow),

$$V'^{t+1}_B = V'^t_{B+1} \quad [10]$$

or if  $CV > 0$  (inflow),

$$V'^{t+1}_B = V'^t_B. \quad [11]$$

It was suspected that the instability might be related to the condition used when  $VD = 0$  (Eqn.8), since it calls for an instantaneous equalizing of properties at the next grid position or location, or an automatic "inflow" condition. The first solution tried was to change the condition to essentially an "outflow" situation, when  $VD = 0$ . Thus Equation [8] was replaced by

$$V'^{t+1}_B = V'^t_{B+1}, \quad [12]$$

and the model was restarted at day 0 with the same temperature input. This change was designed to eliminate any excess "inflow" that might have caused the intense poleward jet and subsequent instability, but after four days of run time, the instability was still there and there was no noticeable change in results from the initial run, out to ten days.

The second change then tried was in the same pattern, but changing back to an "inflow" condition when  $VD = 0$ . Thus, Equation [8] was changed to

$$V'^{t+1}_B = V'^t_B, \quad [13]$$

and the model was again restarted at day 0. Again, after four days of run time, the instability was still there, and there was no noticeable change in results from the initial run, out to ten days. It was therefore apparent that the instability observed was not due to the manner of handling "inflow" and "outflow" at the boundaries when  $VD = 0$ . Nevertheless, a third change was made in the "inflow"/"outflow" condition to improve the handling of the radiation borders. A combination of the first two changes was adopted, in the average form,

$$V'^{t+1}_B = 0.5(V'^t_{B+1} + V'^t_B) \quad [14]$$

and while not solving the problem, it was felt to be a better form than the original [8].

### C. PROBLEM #2

The other possibility for the observed instability lay in the computation of "C", the phase speed. The scheme used to this point for computing CV (i.e., eqn [7] and [9]) is rewritten here,

$$\frac{V_{B+1}^t - V_{B+1}^{t-1}}{\Delta t} = -CV \frac{(V_{B+1}^{t-1} - V_{B+2}^{t-1})}{\Delta y} \quad [15]$$

to show that it really looks like a forward time differencing scheme. The first solution tried was a backward time scheme between the time levels t and t-1. Thus, Equation [15] was replaced by

$$\frac{V_{B+1}^t - V_{B+1}^{t-1}}{\Delta t} = -CV \frac{(V_{B+1}^t - V_{B+2}^t)}{\Delta y}. \quad [16]$$

Once again the model was restarted, with the latest change incorporated in all open boundaries, and once again, the velocity jet inflowing from the south became unstable in four days, with no noticeable improvement.

Another solution was tried, which used a leapfrog scheme based at time zero of the following form:

$$\frac{V_{B+1}^{t+1} - V_{B+1}^{t-1}}{2\Delta t} = -\frac{CV}{\Delta y} \left[ \frac{(V_{B+1}^{t+1} + V_{B+1}^{t-1})}{2} - V_{B+2}^t \right]. \quad [17]$$

This change worsened the instability that was observed in the first runs, and was rejected along with the other unsuccessful conditions, Equations [8], [12], [13], [15] and [16].

A final solution was tried, again using a backward time step between the time levels t+1 and t. Equation [15] was replaced by

$$\frac{V_{B+1}^{t+1} - V_{B+1}^t}{\Delta t} = -CV \frac{(V_{B+1}^{t+1} - V_{B+2}^{t+1})}{\Delta y}. \quad [18]$$

After this change of the boundary conditions, the model was restarted. This time the instability disappeared. The inflow jet from the south was still present but the magnitude did not intensify as in the previous runs. Meridional velocity (V) peaked at 40-50cm/sec while zonal velocity (U) reached 70 cm/sec at a grid location representing

the tightest gradient. This change became the run used for model comparison. More study needs to be done with these boundary conditions to determine the reasons for this instability, and the recommendations section of this thesis suggests several kinds of experiments.

## LIST OF REFERENCES

- Arakawa, A. and V. R. Lamb, 1977: Computational design of the basic dynamical processes of the UCLA general circulation model. *Methods in Computational Physics*, Academic Press, 17, 173-265.
- Batteen, M.L., 1988: Model simulations of a coastal jet and undercurrent in the presence of eddies and jets in the California Current System. *Lecture Note Volume on Poleward Flows on Eastern Boundaries.*, Springer-Verlag (In press).
- Camerlengo, A. L. and J. J. O'Brien, 1980: Open boundary conditions in rotating fluids. *J. Comput. Physics*, 35, 12-35.
- Chelton, D. B., 1984: Seasonal variability of alongshore geostrophic velocity off central California. *J. Geophys. Res.*, 89, 3473-3486.
- Haney, R. L., 1985: Midlatitude sea surface temperature anomalies: a numerical hindcast. *J. Phys. Oceanogr.*, 15, 787-799.
- Hickey, B. M. 1979: The California Current System: hypothesis and facts. *Prog. in Oceanogr.*, 8, 191-279.
- Ikeda, M. and W. J. Emery, 1984: Satellite observations and modeling of meanders in the California Current System off Oregon and Northern California. *J. Phys. Oceanogr.*, 14, 1434-1450.
- Rienecker, M. M., C. N. K. Mooers and A. R. Robinson, 1987: Dynamical interpolation and forecast of the evolution of mesoscale features off Northern California. *J. Phys. Oceanogr.*, 17, 1189-1213.
- Wittmann, P. A., M. M. Rienecker, E. A. Kelley, Jr. and C. N. K. Mooers, 1985: Hydrographic Data from the OPTOMA program; OPTOMA11. *NPS Technical Report, NPS-68-85-011*, Naval Postgraduate School, Monterey, California, 121-152.



## INITIAL DISTRIBUTION LIST

	No. Copies
1. Defense Technical Information Center Cameron Station Alexandria, VA 22304-6145	2
2. Library, Code 0142 Naval Postgraduate School Monterey, CA 93943-5002	2
3. Chairman (Code 68Co) Department of Oceanography Naval Postgraduate School Monterey, CA 93943	1
4. Chairman (Code 63Rd) Department of Meteorology Naval Postgraduate School Monterey, CA 93943	1
5. Dr. M.L. Batteen (Code 68Bv) Department of Oceanography Naval Postgraduate School Monterey, CA 93943	3
6. Dr. R.L. Haney (Code 63Hy) Department of Meteorology Naval Postgraduate School Monterey, CA 93943	3
7. Dr. C.N.K. Mooers, Director Institute for Naval Oceanography Room 322, Bldg. 1100 NSTL, MS 39529	1
8. LCDR Clifford D. Johnson SMC 2098 Naval Postgraduate School Monterey, CA 93943	2
9. Dr. Michele Rienecker Institute for Naval Oceanography Room 322, Bldg. 1100 NSTL, MS 39529	1

10. Director, Naval Oceanography Division 1  
Naval Observatory  
34th and Massachusetts Avenue NW  
Washington, DC 20390
11. Commanding Officer 1  
Fleet Numerical Oceanography Center  
Monterey, CA 93943
12. Commanding Officer 1  
Naval Environmental Prediction Research Facility  
Monterey, CA 93943
13. Naval Ocean Research and Development Activity 1  
NSTL Station  
Bay St. Louis, MS 39522
14. Office of Naval Research (Code 420) 1  
800 N. Quincy Street  
Arlington, VA 22217
15. Dr. A.J. Semtner (Code 68Se) 1  
Department of Oceanography  
Naval Postgraduate School  
Monterey, CA 93943
16. Dr. D.C. Smith IV (Code 68Si) 1  
Department of Oceanography  
Naval Postgraduate School  
Monterey, CA 93943
17. Dr. A.R. Robinson 1  
Center for Earth and Planetary Physics  
Pierce Hall, Harvard University  
Cambridge, MA 02138
18. Dr. S.R. Ramp (Code 68Ra) 1  
Department of Oceanography  
Naval Postgraduate School  
Monterey, CA 93943
19. Ms. A. Bird (Code 68Bd) 1  
Department of Oceanography  
Naval Postgraduate School  
Monterey, CA 93943
20. Dr. K. Bryan 1  
Geophysics Fluid Dynamics Program  
Princeton University GFO4  
Princeton University  
P.O. Box 308  
Princeton, NJ 08540

- |     |  |   |
|-----|--|---|
| 21. | Dr. W. R. Holland<br>National Center for Atmospheric Research (NCAR)<br>P.O. Box 3000<br>Boulder, CO 80307 | 1 |
| 22. | Dr. J. Allen<br>College of Oceanography<br>Oregon State University<br>Corvallis, OR 97331                  | 1 |
| 23. | Director of Research Administration (Code 012)<br>Naval Postgraduate School<br>Monterey, CA 93943          | 1 |













Thesis  
J57451 Johnson  
J5 c.1  
c.

Numerical ocean pre-  
diction in the Califor-  
nia coastal region using  
a high-resolution pri-  
mitive equation model.  
29 JUL 92 37547

Thesis  
J57451 Johnson  
c.1 Numerical ocean pre-  
diction in the Califor-  
nia coastal region using  
a high-resolution pri-  
mitive equation model.





W0557451  
Numerical ocean prediction in the Califo



3 2768 000 84938 4  
DUDLEY KNOX LIBRARY